Biochemical Pharmacology 250 (2026) 118037

Contents lists available at ScienceDirect

Biochemical Pharmacology

journal homepage: www.elsevier.com/locate/biochempharm

Diving into AA9-mediated transglutaminase 2 inhibition reveals ferroptosis as driver of anticancer effects

Pietro Ancona [a,1], Silvia Grassilli [b,c,1], Cristina Zuccato [a], Cinzia Brenna [a,d], Davide Barboni [e], Alberto Cavazzini [e], Martina Catani [e], Valeria Bertagnolo [a], Pauline Navals [f], Jocelyn A. Menard [g], Jeffrey C. Smith [g,h], Carlo M. Bergamini [i], Nicoletta Bianchi [a,*], Jeffrey W. Keillor [f,1], Luca M. Neri [a,d,1]

[a] Department of Translational Medicine, University of Ferrara 44121, Ferrara, Italy
[b] Department of Environmental and Prevention Sciences, University of Ferrara 44121, Ferrara, Italy
[c] Laboratory for Advanced Therapy Technologies (LTTA), University of Ferrara 44121 Ferrara, Italy
[d] Laboratory for Advanced Therapy Technologies (LTTA)-Electron Microscopy Center, University of Ferrara 44121 Ferrara, Italy
[e] Department of Chemical, Pharmaceutical and Agricultural Sciences, University of Ferrara 44121 Ferrara, Italy
[f] Department of Chemistry and Biomolecular Sciences, University of Ottawa, Ottawa K1N 6N5, Canada
[g] Department of Chemistry and Institute of Biochemistry, Carleton University, Ottawa K1S 5B6, Canada
[h] Carleton Mass Spectrometry Centre, Carleton University, Ottawa, Ontario K1S 5B6, Canada
[i] Department of Neuroscience and Rehabilitation, University of Ferrara 44121 Ferrara, Italy

ARTICLE INFO

Keywords:
Transglutaminase 2
TG2 inhibitor
AA9
Ferroptosis
Breast cancer

ABSTRACT

Ferroptosis recently gained considerable attention in breast cancer research, particularly in triple-negative subtypes. In this context, emerging evidence links transglutaminase 2 (TG2) to aggressive tumour phenotypes, highlighting pharmacological TG2 inhibition as a promising therapeutic approach in aggressive breast cancer settings.

Comparative analysis of independent RNA-sequencing datasets from distinct cellular models treated with irreversible TG2 inhibitors revealed ferroptosis as the only significantly enriched and commonly deregulated process. In triple-negative breast cancer cells, treatment with the cell-permeable AA9 inhibitor triggered a coherent ferroptotic transcriptional program, characterized by downregulation of glutathione peroxidase 4 and

Abbreviations: ACN, Acetonitrile; ACTB, β-actin; ALDOA, Aldolase A; AKT1, RAC-alpha serine/threonine-protein kinase; ARNT, Aryl Hydrocarbon Receptor Nuclear Translocator; ATG101, Autophagy Related 101; BAX, Bcl-2-associated X protein; BID, BH3 Interacting Domain Death Agonist; Boc, *tert*-butyloxycarbonyl; CCNB1, Cyclin B1; CDK1, Cyclin-dependent kinase 1; CDKN1A, cyclin dependent kinase inhibitor 1A; CDKN1B, cyclin dependent kinase inhibitor 1B; CDKN3, Cyclin-dependent kinase inhibitor 3; CHAC1, Glutathione-specific gamma-glutamylcyclotransferase 1; CRC, colorectal carcinoma; DCM, dichloromethane; DEGs, differentially expressed genes; DIPEA, N,N'-diisopropylethylamine; DMSO, dimethyl sulfoxide; EMT, epithelial–mesenchymal transition; ENO1, Enolase 1; ESI, Electrospray ionisation; Et_2O, diethyl ether; EtOAc, Ethyl acetate; FDR, False Discovery Rate; FTH, Ferritin heavy chain; FTL, Ferritin light chain; GAPDH, (glyceraldehyde-3-phosphate dehydrogenase); GCLM, Glutamate-Cysteine Ligase Modifier Subunit; GEO, Gene Expression Omnibus; GPX4, Glutathione peroxidase 4; GSH, glutathione; GSS, Glutathione synthetase; HATU, hexafluorophosphate azabenzotriazole tetramethyl uronium; HDAC1, Histone deacetylase 1; HIF, Hypoxia-inducible factor; HMOX1, Heme Oxygenase 1; H_2O_2, hydrogen peroxide; HOAc, Acetic acid; HPLC, High Performance Liquid Chromatography; HRMS, High-Resolution Mass Spectrometry; IgG, Immunoglobulin G; IL-4, Interleukin 4; LC–MS/MS, liquid chromatography–tandem mass spectrometry; LDHA, Lactate dehydrogenase A; MAP1LC3B, Microtubule-associated proteins 1A/1B light chain 3B; MeOH, methanol; mTOR, mechanistic target of rapamycin; NFE2L2, Nuclear factor, erythroid 2-like 2; NMR, Nuclear Magnetic Resonance; NOESY, Nuclear Overhauser Effect Spectroscopy; ORA, Over-representation analysis; PBS, phosphate-buffered saline; PMA, Phorbol 12-myristate 13-acetate; PTFE, Polytetrafluoroethylene; QTOF, quadrupole time-of-flight; ROS, Reactive oxygen species; RSL3, RAS-selective lethal 3; RT-qPCR, reverse transcription quantitative polymerase chain reaction; SD, standard deviation; SEA, Similarity Ensemble Approach; SLC7A11, Solute Carrier Family 7 Member 11; SQSTM1, Sequestosome 1; STP, Swiss Target Prediction; TEM, Transmission Electron Microscopy; TFA, trifluoracetic acid; TG2, Transglutaminase 2; TG2 KO MEFs, Transglutaminase 2 knockout mouse embryonic fibroblasts; TLC, Thin-layer chromatography; TN, TargetNet; TNBC, triple-negative breast cancer; TXNRD1, Thioredoxin Reductase 1.

* Corresponding author at: Department of Translational Medicine, University of Ferrara, Complesso per la Didattica e la Ricerca - CUBO - Secondo piano, via Fossato di Mortara, 70 c.o. viale Eliporto, 44121 Ferrara, Italy.
E-mail address: nicoletta.bianchi@unife.it (N. Bianchi).
[1] These authors contributed equally to this work.

https://doi.org/10.1016/j.bcp.2026.118037
Received 21 February 2026; Received in revised form 1 May 2026; Accepted 5 May 2026
Available online 9 May 2026
0006-2952/© 2026 The Author(s). Published by Elsevier Inc. This is an open access article under the CC BY license (http://creativecommons.org/licenses/by/4.0/).

the glutathione biosynthesis genes and by upregulation of stress-responsive and iron-handling factors. A covalent pull-down magnetic system combined with proteomics and bioinformatic target prediction identified TG2 as the primary intracellular target of AA9 and revealed a TG2-centered interactome involving, among the pathways, hypoxia signalling, cytoskeletal regulation, and apoptosis. Moreover, molecular docking and immunoprecipitation experiments demonstrated that TG2 is physically associated with BH3-interacting domain death agonist and Bcl-2-associated X protein, key mediators of ferroptosis and apoptosis. Transmission electron microscopy further confirmed that AA9 induced ferroptosis-associated mitochondrial alterations, prevented by ferrostatin-1 co-treatment.

Overall, these findings confirm TG2 pharmacological targeting as a strategy to reprogram metabolic adaptation and cell death responses in aggressive tumour subtypes.

1. Introduction

In breast cancer, the process of cell death mediated by ferroptosis is attracting increasing interest, and its inducers are under investigation to determine the associated molecular pathways [1]. In triple-negative breast cancer (TNBC), the targeting of ferroptosis-related proteins, using GPX4 (glutathione peroxidase 4) inhibitors, represents a useful strategy to slow down tumour growth and enhance the potential of immune-combined therapies [2]. In addition, the development of nanoparticle-based delivery systems containing ferroptosis-inducing drugs has been shown to improve their clinical potential and therapeutic efficacy [3].

The relationship between transglutaminase 2 (TG2) and ferroptosis has been investigated in recent years in transglutaminase 2 knockout mouse embryonic fibroblasts (TG2 KO MEFs), a cellular model employed to explore the biological functions of this enzyme in several processes, including autophagy, apoptosis, differentiation, and resistance to oxidative stress [4]. The authors have shown that TG2 KO MEFs exhibit increased resistance to canonical ferroptosis inducers such as RAS-selective lethal 3 (RSL3) and erastin, followed by a marked decrease in lipid peroxidation. Mechanistically, this phenotype does not appear to be explained by several established ferroptosis-related pathways, such as aldo–keto reductases or arachidonate lipoxygenases 12/15. Similarly, despite the known involvement of TG2 in autophagy, no clear evidence supports a role for ferritinophagy in TG2-deficient cells. Moreover, ferroptosis suppressor protein 1 and the GTP cyclohydrolase 1/tetrahydrobiopterin axis do not appear to account for the ferroptosis-resistant phenotype. Overall, although TG2 could participate in the pathway leading to ferroptosis execution, the precise molecular mechanisms remain to be fully elucidated [5], as well as the downstream molecular targets of TG2. In this context, TG2 knockdown should be interpreted with caution, as it may represent a non-physiological condition associated with adaptive responses, including genetic compensation. Other findings sustain that TG2 seems to indirectly modulate ferroptosis by promoting autophagic activity [6], including ferritinophagy with consequent degradation of ferritin. Finally, TG2 can act as an epigenetic modulator [7] by modifying nuclear proteins or transcription factors, thereby altering gene expression and favouring either cell survival or cell death.

Based on this rationale, pharmacological inhibition of TG2 could provide a strategic approach to explore the downstream biological consequences of its blockage. In breast cancer, TG2 is predominantly expressed in cells displaying mesenchymal-like features, particularly within TNBCs [8], which represent some of the most aggressive and therapeutically challenging tumour subtypes. TG2 has recently emerged as a promising biomarker associated with mesenchymal circulating tumour cells [9]. Consequently, molecules capable of limiting its functions are gaining interest as potential therapeutic agents.

AA9 has been validated as a cell-permeable, irreversible inhibitor that blocks both the transamidase and G-protein activities of TG2 [10]. In breast cancer cells, especially *TP53*-mutated triple-negative phenotypes (e.g., MDA-MB-231 and MDA-MB-436), AA9 induces apoptosis, inhibits migration and invasiveness, and alters key metabolic and signalling networks, including Hypoxia-inducible factor (HIF)-related, RAC-alpha serine/threonine-protein kinase (AKT)/mechanistic target of rapamycin (mTOR), integrin, and p53-mediated pathways [11], and metabolomic profiling further discloses a significant impact on glutamate/aspartate metabolism [12].

Hypoxia deeply influences cancer cell sensitivity to ferroptosis by driving metabolic rewiring, a process reminiscent of the Warburg effect, characterized by a shift toward glycolysis at the expense of oxidative phosphorylation. In this context, activation of HIF-1/2α remodels iron and lipid metabolism and often decreases susceptibility to ferroptosis through the upregulation of SLC7A11 (solute carrier family 7 member 11) [13], a key component of the cystine/glutamate antiporter system xCT. This transporter promotes the uptake of extracellular cystine in exchange for intracellular glutamate, thereby increasing intracellular glutathione (GSH) levels. Moreover, glutamate/aspartate metabolism and amino acid flux are tightly interconnected with cellular redox regulation, and efficient GSH production is essential for neutralizing reactive oxygen species (ROS) and preventing lipid peroxidation [14].

In this study, we first analyzed several RNA-sequencing datasets with comparable characteristics derived from cellular models to assess whether TG2 inhibition triggered common changes. Subsequent experiments converged on breast cancer, considering that conventional treatments often promote the selection of resistant cell populations that compromise treatment outcomes. We aimed to elucidate the functional contribution of TG2 within the molecular framework of the intricate crosstalk between hypoxia signalling, metabolic adaptation, and modulation of susceptibility to ferroptosis.

2. Methods

2.1. Bioinformatics analysis of RNA-sequencing data

We gathered RNA-sequencing data both from publicly available datasets and from our previous experiments. First, we analyzed RNA-sequencing data derived from samples of human monocytic THP-1 cells, obtained from a patient affected by acute monocytic leukemia. These cells were differentiated into macrophages using phorbol 12-myristate 13-acetate (PMA) and subsequently polarized toward M1 or M2 phenotypes using appropriate stimuli (Interleukin 4, IL-4), then treated with the irreversible TG2 inhibitor Z-DON. Data were retrieved from the Gene Expression Omnibus (GEO) under accession number GSE222284 [15]. Secondly, transcriptomic datasets from MDA-MB-231 and MDA-MB-436 cell lines, untreated or treated with AA9, were obtained from our previous study [11].

The quality of the raw FASTQ files was assessed using FastQC v0.12.1 (https://www.bioinformatics.babraham.ac.uk/projects/fastqc/). Reads were aligned to the GRCh38/hg38 human reference genome using STAR v2.7.11b [16] with default settings and the quantMode flag enabled. Aligned files were imported into RStudio v4.5.2 (Posit Software, PBC, Boston, MA) and merged into a single count matrix used for differential gene expression analysis with the DESeq2 package [17].

Significantly common deregulated genes (False Discovery Rate, FDR $\leqslant 0.05$) in the paired samples (treated *versus* untreated) underwent an Over-Representation Analysis (ORA), using the KEGG gene collection implemented in WebGestalt v2024 [18].

Finally, meaningful functional interactions among the differentially expressed genes (DEGs) were visualized through a protein–protein interaction network generated with the STRING platform v12.0 [19].

2.2. Cell lines

The breast cancer cell lines, MDA-MB-436 (RRID: CVCL_0623) and MDA-MB-231 (RRID: CVCL_0062), were employed in our assays and cultured as previously published [11]. The presence of mycoplasma was tested before conducting the experiments. In the treatment, we used 50 μM AA9 for 24 h, and 0.1% dimethyl sulfoxide (DMSO, Merck KGaA, Darmstadt, Germany), as a vehicle.

2.3. Transfection experiments for TG2 silencing by siRNA

MDA-MB-231 cells were seeded in 6-well plates (one well per experimental condition) and transfected with TG2-specific siRNA using a DharmaFECT (Dharmacon, Horizon Discovery, CarloErba, Cornaredo, MI, Italy) transfection reagent optimized for this cell line, according to the manufacturer's instructions. The siRNA molecule was designed using Horizon Discovery tool (https://horizondiscovery.com/) specifically recognizing TG2 full-length isoform. The sequence of the duplex siRNA is: sense: 5'-G.G.A.G.G.A.A.G.U.U.A.A.G.G.U.G.A.G.A.A.U.U-3' and antisense: 5'-P.U.C.U.C.A.C.C.U.U.A.A.C.U.U.C.C.U.C.C.U.U-3' (transcript position nt 2007–2025 in NM_004613.4, *TGM2* variant 1). It was resuspended in RNase-free buffer and used at 500 nM, complexed with the transfection reagent in serum-free medium to allow the formation of siRNA–lipid complexes. Cells were then exposed to the transfection mixture in medium without antibiotics. Control cells were treated with transfection reagent alone (DharmaFECT) without siRNA. After incubation for 30 h, cells were collected and processed for gene expression analysis.

2.4. Cell cycle assay

The cells were seeded in 12-well plates in 1 mL of medium. After treatment, cells were detached using trypsin (Euroclone, Pero, MI, Italy), inactivated with fresh medium containing Fetal Bovine Serum (Merck KGaA), centrifuged at 1200 rpm for 5 min, washed with phosphate-buffered saline (PBS) solution (Merck KGaA), and fixed in 70% ethanol overnight. Before testing, the cells were washed once in PBS and resuspended in 200 μL of Muse™ Cell Cycle Reagent (Prodotti Gianni, Milano, Italy); then, data were acquired by Muse™ Cell Analyzer.

2.5. Assessment of ATP levels

In these experiments, the inhibitors AA9 and NCEG2 were administered at 50 μM for 8 and 24 h. This assay was performed using the CellTiter-Glo® Luminescent Cell Viability Assay (Promega, Madison, WI, USA) according to the manufacturer's instructions, and luminescence was measured using the GloMax® Discover Instrument (Promega).

2.6. Transmission Electron Microscopy analysis

For Transmission Electron Microscopy (TEM), samples were fixed in 2.5% glutaraldehyde (Merck KGaA) in 0.1 M phosphate buffer (pH 7.2) for 2 h at room temperature. Following three washes in the same buffer, secondary fixation was performed using 1% osmium tetroxide (Electron Microscopy Sciences, Morgantown, PA, USA) in 0.1 M cacodylate buffer (pH 7.2) for 2 h at RT. Dehydration was carried out using an ascending acetone series (50%, 75%, 90%, 100%) before embedding in Durcupan™ ACM resin (Merck KGaA). Resin blocks were polymerized at 60°C for 72 h and subsequently sectioned at a thickness of 70 nm using an ultramicrotome. Ultrathin sections were mounted on collodion-coated 150-mesh copper grids and contrasted with Uranyless and lead citrate (Electron Microscopy Sciences). Imaging was performed using a Talos L120C TEM (Thermo Fisher Scientific, Waltham, Massachusetts, USA) at a resolution of 4096 × 4384 pixels with a 1 s exposure time.

Table 1
Primers used in gene expression analysis by qPCR. Oligonucleotides sequences designed using Primer-BLAST software (site https://www.ncbi.nlm.nih.gov/tools/primer-blast, accessed on 6 October 2025).

Gene name	Forward primer	Reverse primer
HMOX1	5′-TAGAAGAGGCCAAGACTGCG-3′	5′-TCCTTGGTGTCATGGGTCAG-3′
FTH1	5′-ACTACCACCAGGACTCAGAGG-3′	5′-CCTGAAGGAAGATTCGGCCA-3′
GPX4	5′-ATTGGTCGGCTGGACGAG-3′	5′-TCGATGTCCTTGGCGGAAAA-3′
SQSTM1	5′-CCGTGAAGGCCTACCTTCTG-3′	5′-TCCTCGTCACTGGAAAAGGC-3′
BID	5′-GGAGGAAGCGGGTAGTCG-3′	5′-GGAACCGTTGTTGACCTCAC-3′
NFE2L2	5′-AGAAACCAGTGGATCTGCCA-3′	5′-TGACTGAAACGTAGCCGAAG-3′
ATG101	5′-TCCAGCTTCCGAGTCCAG-3′	5′-CTTCACCCTACCCAAGGGC-3′
GSS	5′-GAAAGGCGAACTAGTGTTGGG-3′	5′-TGAATGGGGCATAGCTCACC-3′
CHAC1	5′-GTGGTGACGCTCCTTGAAGA-3′	5′-GCCAATGCCTTCAGTGGTTG-3′
ARNT	5′-CTACTGCCAACCCCGAAATG-3′	5′-CTGGCAAACCGCTCCTTATC-3′
HIF1A	5′-ACCGATTCACCATGGAGGG-3′	5′-GCCTCATCACAGAGGCCTTA-3′
ALDOA	5′-TTTCCTTTCCCCCAGTTGCC-3′	5′-CGGGGTCAGTGCTGGATATT-3′
LDHA	5′-CCGATTCCGGATCTCATTGC-3′	5′-AGCACCAACCCCAACAACT-3′
ENO1	5′-CCTGCCCTGGTTAGCAAGAA-3′	5′-GGCGTTCGCACCAAACTTAG-3′
CDK1	5′-GGCTCTTGGAAATTGAGCGG-3′	5′-CATGGCTACCACTTGACCTGT-3′
CDKN1A	5′-AGTCAGTTCCTTGTGGAGCC-3′	5′-CATTAGCGCATCACAGTCGC-3′
CDKN1B	5′-GTGCGAGTGTCTAACGGGAG-3′	5′-AGCCGGAGCCCCAATTAAAG-3′
CDKN3	5′-GGACTCCTGACATAGCCAGC-3′	5′-TGATGGTCTGTATTGCCCCG-3′
CCNB1	5′-AAGGCGAAGATCAACATGGCA-3′	5′-GGGCTTGGAGAGGCAGTATC-3′
AKT1	5′-GCGTGACCATGAACGAGTTT-3′	5′-CTTGGCCACGATGACTTCCT-3′
AKT2	5′-ACAAGGAAAGGGAACCAGCG-3′	5′-GGTACGCTGTCACCTAGCTC-3′
AKT3	5′-GCAAAGGATGAAGTGGCACA-3′	5′-ACCCGCTCTCTCGACAAATG-3′
ACTB	5′-CATTGCCGACAGGATGCA-3′	5′-GCTGATCCACATCTGCTGGA-3′
GAPDH	5′-GAAGGTCGGAGTCAACGGATT-3′	5′-AGCATCGCCCCACTTGATT-3′

2.7. RNA extraction, reverse transcription, and quantitative polymerase chain reactions

Samples were derived from MDA-MB-436 and MDA-MB-231 breast cancer cells treated for 24 and 48 h with 50 μM AA9 or 0.1% DMSO (Merck KGaA), as a vehicle. Each sample was obtained from a flask containing cells at 80% confluence, collected by centrifugation at 1200 rpm for 10 min at 4°C, washed three times with PBS, and then lysed in TRI Reagent (Merck KGaA). RNA was purified according to the manufacturer's instructions, as described by Ancona *et al.* [11] and quantified using the spectrophotometer DeNovix DS-11 (DeNovix Inc., Wilmington, DE, USA), resuspended in RNA/DNA nuclease-free water, and 1 μg of total RNA used in reverse transcription conducted with TaqMan™ Reverse Transcription Reagents kit (Thermo Fisher Scientific). Fifty ng

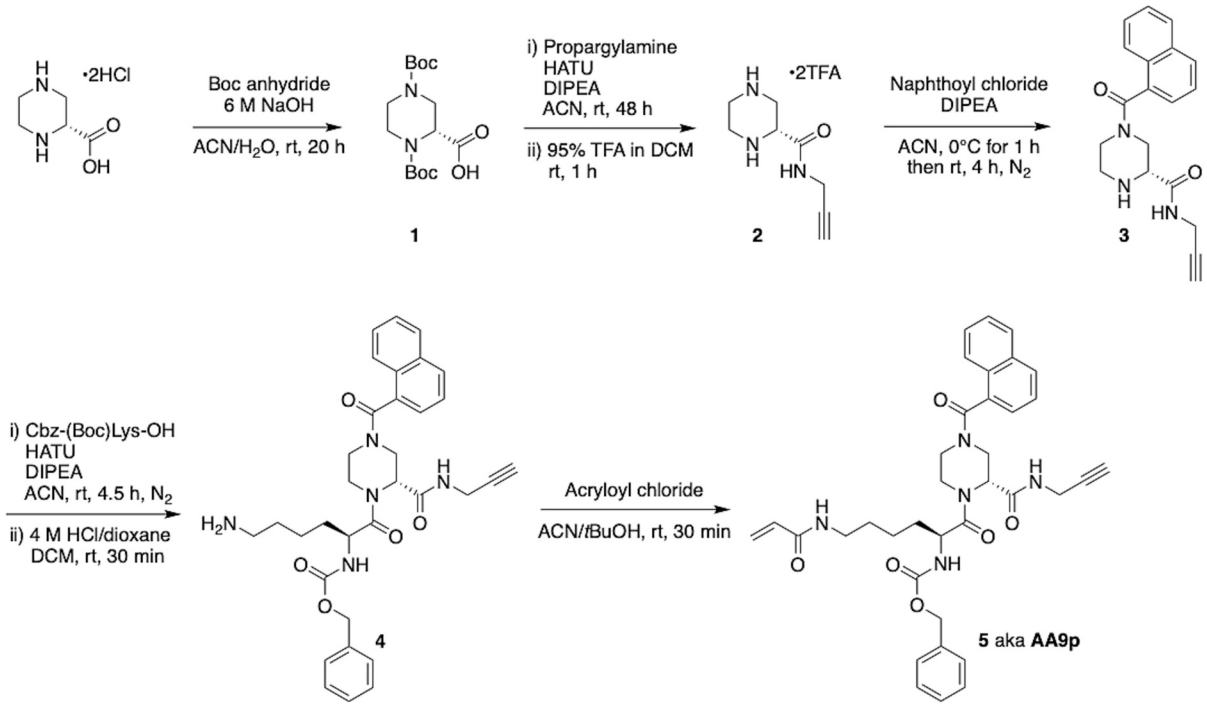

Scheme 1. Synthetic route for the synthesis of covalent inhibitor **AA9p**.

of cDNA were amplified in each reaction by PowerUp™ SYBR® Green Master Mix (Thermo Fisher Scientific) and the thermal cycler CFX96 Touch™ Real-Time PCR Detection System (Bio-Rad Laboratories, Segrate, Milan, Italy). Fold Change gene expression of specific targets was quantified in control and treated samples by applying the formula $2^{-\Delta CT}$, considering the geometric mean between two housekeeping genes, *β-actin* (*ACTB*) and *glyceraldehyde-3-phosphate dehydrogenase* (*GAPDH*). The primer sequences were designed using the web tool site Primer-BLAST (https://www.ncbi.nlm.nih.gov/tools/primer-blast, accessed on 6 October 2025) and reported in Table 1.

2.8. Immunoprecipitation experiments and Western blot analysis

Protein content in the cellular extract was quantified using the BCA Protein Assay Kit (Bio-Rad Laboratories). For immunoprecipitation experiments, MDA-MB-436 cells were treated with CHAPS-Immunoprecipitation Buffer, prepared following a previously described procedure [20], treated with protease and phosphatase inhibitors, and incubated with antibodies against TG2 (cat. A036, Zedira, Darmstadt, Germany) and BID (BH3 Interacting Domain Death Agonist, cat. 10988-1-AP, Proteintech Europe, Manchester, UK). Immunocomplexes were collected by absorption with protein A-Sepharose (Pharmacia, Uppsala, Sweden), according to the previously reported experimental conditions [8].

For Western blot analysis, lysates of MDA-MB-436 cells treated with 50 μM AA9 or 0.1% DMSO for 48 h were obtained by the addition of Laemmli's sodium dodecyl sulfate sample buffer, after washing of the cells with cold PBS containing 1 mM sodium orthovanadate. The protein content was quantified by BCA Protein Assays (Thermo Fisher Scientific), and 15 μg of total lysates were employed.

Immunoprecipitates using antibodies against TG2 (Zedira) and BID (Proteintech Europe) were separated on 12.5% denaturing polyacrylamide gel and blotted to nitrocellulose membranes (GE Healthcare Life Science, Little Chalfont, UK). Hybridization reactions were carried out using primary rabbit antibodies anti-BID, anti-BAX (anti-Bcl-2-associated X protein, cat. 41162S, Cell Signalling Technology, Danvers, MA, USA), anti-SLC7A11/xCT (cat. 26864-1-AP, Proteintech Europe), and primary mouse antibodies anti-TG2 (Zedira), anti-HMOX1 (Heme Oxygenase 1, cat. sc-136960, Santa Cruz Biotechnology, Santa Cruz, CA, USA), anti-FTH (Ferritin heavy chain, cat. sc-376594, Santa Cruz Biotechnology), anti-AKT2 (cat. #3063, Cell Signaling Technology) and p-AKT2 (Ser474, cat. #8599, Cell Signaling Technology), and anti-actin (cat. A4700, Merck KGaA); while a non-specific Immunoglobulin G (IgG) was used as the negative control (cat. sc-53344, Santa Cruz Biotechnology). Then, membranes were incubated with peroxidase-conjugated species-specific secondary antibodies and revealed with the ECL system (Cyanagen, Bologna, Italy).

The chemiluminescence of the resolved bands was acquired with an ImageQuantTM LAS 4000 biomolecular imager (GE Healthcare Life Science), and densitometric analysis was performed by Image Quant TL software (GE Healthcare Life Science), as previously reported [21]. The results were expressed as means ± SD of three independent experiments. Statistical analysis was performed by a two-tailed Student's *t*-test for unpaired data using the GraphPad Prism 6.0 statistical package (GraphPad Software, San Diego, CA, USA). P value < 0.05 was considered statistically significant.

2.9. Docking analysis: protein-protein interactions

To predict the interactions between TG2 and the putative partner proteins, we performed molecular docking analyses using HADDOCK v2.4 software (available at https://rascar.science.uu.nl/haddock2.4/, last accessed on 19/11/2025), with default parameters.

The 3D structures of the proteins included in the study were obtained from the RCSB Protein Data Bank (https://www.rcsb.org/). Accession codes 2Q3Z and 4PYG were used for the open and closed conformations of TG2, while 2BID and 6EB6 were used for BID and BAX.

Before docking, all structure files were pre-processed and validated using pdb-tools v2.3.1 (https://rascar.science.uu.nl/pdbtools/, last accessed on 19/11/2025), employing the 'pdb_selaltloc' and 'pdb_validate' functions.

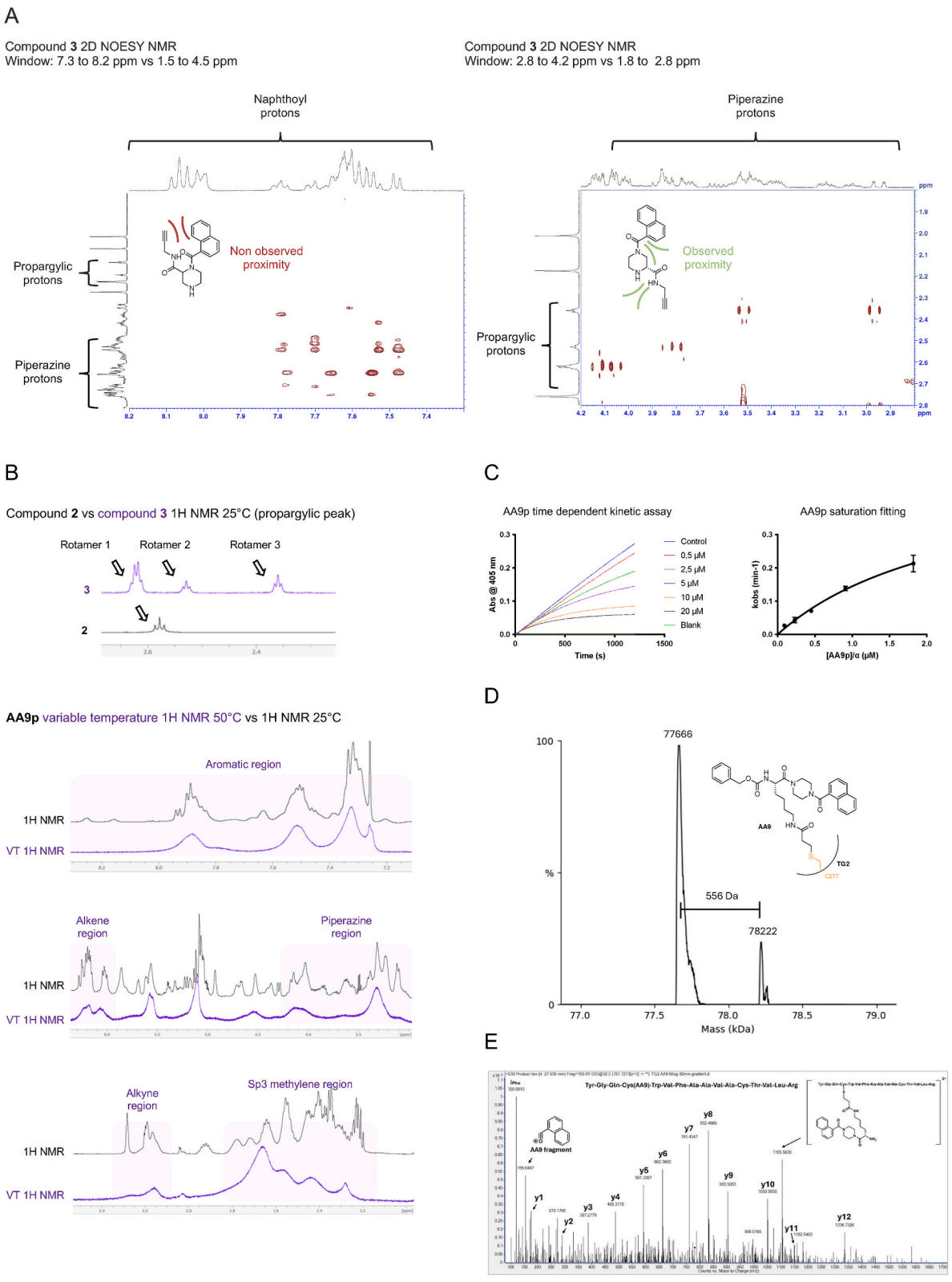

Fig. 1. A. 2D NOESY NMR analysis. Left window (7.3–8.2 ppm *vs* 1.5–4.5 ppm) shows proximity coupling signals of the naphthoyl aromatic protons with the piperazine and propargylic protons, respectively. Right window (2.8–4.2 ppm *vs* 1.8–2.8 ppm) shows proximity coupling signals between the propargylic and piperazine protons. **B. Rotamers of compound 3 and AA9p.** The ^{1}H NMR alkyne peak in **2** (black) and **3** (purple) shows the presence of three distinct rotamers once the piperazine linker is functionalized with naphthoyl group (top). The VT NMR analysis of **AA9p** at 25°C (black) and 50°C (purple) showing coalescence of rotamer peaks (bottom). **C. Kinetic evaluation of AA9p.** Left, time-dependent inhibition providing observed rate constants (k_{obs}) of inactivation of human TG2. Right, hyperbolic fitting of k_{obs} *vs* [AA9p] to a saturation kinetics model. **D. Intact mass analysis.** The deconvoluted (UniDec) intact mass spectrum of TG2 after reaction with inhibitor **AA9** showing a 556-Da mass increase compared to its unbound state. **E. MS/MS analysis.** Following collision-induced dissociation at 32.3 eV, the MS/MS spectrum of the TG2 tryptic peptide (residues 274–289, *m/z* 781.7213) shows modification of the C277 residue with all major product ions annotated, including AA9-specific ions at *m/z* 155.0487 (Δppm = − 3.2) and *m/z* 1105.5630 (Δppm = 3.1).

2.10. Use of propargylated inhibitor AA9p as a probe for target fishing, proteomics, and applied bioinformatics analysis

2.10.1. Chemical synthesis of AA9p

AA9p was synthesized according to the route shown in Scheme 1. The bis-protection of commercially available (*R*)-piperazine carboxylic acid, using Boc-anhydride, yielded compound **1**. The subsequent condensation of **1** with propargylamine was followed directly by Boc removal using trifluoracetic acid (TFA) to give the diamine salt **2**. This diamine was then reacted with less than one equivalent of naphthoyl chloride, under strict temperature and time control, to allow for the formation of the preferred regioisomer **3**. The condensation of **3** and α-benzyloxycarbonyl-(∈-Boc)-lysine, followed by removal of the Boc group, provided amine **4**. Finally, the acrylamide warhead was introduced by reaction with acryloyl chloride, leading to the final compound **5** aka **AA9p**.

Solvents and reagents for the synthesis of **AA9p** were all purchased from Millipore-Sigma (Oakville, ON, Canada) unless indicated otherwise, and used directly without further purification. All ^{1}H- and ^{13}C-Nuclear Magnetic Resonance (NMR) spectra were recorded on 300-400 and 600-MHz Bruker spectrometers, respectively, and all chemical shifts are reported in ppm referenced to the deuterated solvent peak. High-resolution mass spectra (HRMS) were obtained with a quadrupole time-of-flight (QTOF) analyzer and electrospray ionization (ESI). Thin-layer chromatography (TLC) was performed using aluminum-backed silica plates and visualized using UV light unless specified differently.

*(2R)-1,4-bis[(tert-butoxy)carbonyl]piperazine-2-carboxylic acid **(1)***

R-piperazine carboxylic acid (CombiBlock, San Diego, CA, USA) (0.5 g, 2.45 mmol, 1 eq), Boc anhydride (Oakwood Chemicals, Estill, SC, USA) (2.140 g, 9.9 mmol, 4 eq) and 6 M NaOH (3.2 mL, 8 eq) were dissolved in a mixture of water and acetonitrile (ACN, 70/30, 50 mL) and stirred at room temperature until reaction completion (20 h), followed by TLC, methanol (MeOH)/ dichloromethane (DCM) 10/90 + ninhydrin stain, 20 h. The ACN was then evaporated, and the resulting aqueous phase was washed with diethyl ether (Et_2O, 3 × 50 mL). The pH was adjusted to around 3 and the desired compound was extracted with ethyl acetate (EtOAc, 6 × 50 mL). The organic solvent phase was then dried over anhydrous $MgSO_4$, filtered, and evaporated, leading to the desired product as a white powder in a 91% yield. ^{1}H-NMR (300 MHz, $CDCl_3$): 1.43 (9H, s), 1.47 (9H, s), 2.85 (1H, broad s), 3.09 (1H, d, *J*=14.53 Hz), 3.23 (1H, m), 3.83 (1H, dd, *J*=12.81, 35.47 Hz), 4.00 (1H, broad s), 4.55 (1H, m), 4.67 (1H, d, *J*=60.05 Hz). ^{13}C-NMR (75 MHz, $CDCl_3$): 155.8, 155.2, 154.6, 81.0, 80.7, 60.5, 54.8, 53.5, 41.5, 40.2, 28.8, 28.3, 14.2. HRMS: $[M + Na]^+$ calculated = 353.1660, found = 353.1662.

*(2R)-N-(prop-2-yn-1-yl)piperazine-2-carboxamide; 2,2,2-trifluoroacetic acid **(2)***

1 (0.15 g, 0.45 mmol, 1.1 eq), hexafluorophosphate azabenzotriazole tetramethyl uronium (Oakwood Chemicals, Estill, SC, USA) (HATU, 0.25 g, 0.66 mmol, 1.6 eq) and *N,N'*-diisopropylethylamine (DIPEA, 0.096 mL, 0.82 mmol, 2 eq) were dissolved in ACN (2 mL) and propargylamine (CombiBlock, San Diego, CA, USA) (0.025 mL, 0.41 mmol, 1 eq) was added. The reaction was stirred at room temperature for 48 h until completion (TLC system: hexane/EtOAc 70/30 + ninhydrin stain, 48 h). The ACN was then evaporated, and the resulting crude oil was dissolved in EtOAc (10 mL) and washed with 10% acetic acid (HOAc, 3 × 10 mL), brine (a saturated solution of NaCl, 1 × 10 mL), saturated $NaHCO_3$ (3 × 10 mL) and brine again (3 × 10 mL) before being dried over anhydrous $MgSO_4$, filtered and concentrated. The resulting crude material was directly dissolved in a large excess mixture of TFA in DCM (95/5, 5 mL) and the reaction was stirred at room temperature until completion (1 h) (TLC system DCM/MeOH 95/5 + ninhydrin stain, 1 h). The solvents were evaporated and the TFA was removed through co-evaporation with DCM (6 × 10 mL). The desired product was precipitated in Et_2O, leading to compound **2** in a 77% yield. ^{1}H NMR (400 MHz, D_2O): 1.10 (1H, t, *J*=7.08 Hz), 2.58 (1H, t, *J*=2.55 Hz), 3.33-3.52 (4H, m), 3.67 (1H, dd, *J*=5.37 Hz), 3.77 (1H, dd, *J*=4.39 Hz), 3.88 (1H, dd, *J*=4.43 Hz), 3.97 (2H, d, *J*=2.5 Hz), 4.39 (1H, dd, J=5.14 Hz). ^{13}C-NMR (101MHz, D_2O): 29.1, 39.5, 39.8, 42.3, 53.3, 72.4, 78.5, 164.4. HRMS: $[M + H]^+$ calculated = 168.1111, found = 168.1113.

*(2R)-4-(naphthalene-1-carbonyl)-N-(prop-2-yn-1-yl)piperazine-2-carboxamide **(3)***

Compound **2** (0.1 g, 0.25 mmol, 1 eq) and DIPEA (0.096 mL, 0.25 mmol, 1 eq) were both dissolved in ACN, then cooled to 0°C under nitrogen atmosphere for 1 h. Naphthoyl chloride (34.7 μL, 0.23 mmol, 0.9 eq) was then added drop-wise to the reaction mixture, which was subsequently stirred at room temperature for 4 h. The ACN was then evaporated, and the resulting crude oil was directly purified by reverse phase flash chromatography, leading to compound **3** with a yield of 49%. ^{1}H-NMR (600 MHz, D_2O): 2.01, 2.17 & 2.76 (1H, s, s, s), 2.36, 2.53 & 2.62 (1H, t, t, t), 2.92-2.96 & 3.02-3.21 (1H, dd & m), 3.27-3.67 (3H, m), 3.68-3.94 (2H, m), 4.00-4.18 (2H, m), 4.37-4.87 (1H, m), 4.62-4.74 (1H, 2 x dd, *J*=6.10 Hz), 7.47-7.57 (1H, m), 7.57-7.67 (3H, m), 7.67-7.81 (1H, m), 7.99-8.08 (2H, m). ^{13}C-NMR (151MHz, D_2O): 29.1, 38.5, 41.4, 43.5, 46.6, 55.0, 72.3, 123.7, 124.5, 125.2, 125.4, 127.0, 127.9, 128.7, 130.5, 130.8, 133.2, 165.5, 171.9. HRMS: $[M + H]^+$ calculated = 322.1529, found = 322.1523.

The regioselectivity of this reaction was also assessed by NOESY (Nuclear Overhauser Effect Spectroscopy) NMR, showing that the propargylic protons do not engage in through-space coupling with the naphthoyl aromatic protons (Fig. 1A), which would be expected if the unwanted isomer were formed.

*benzyl N-{6-amino-1-[(2R)-4-(naphthalene-1-carbonyl)-2-[(prop-2-yn-1-yl)carbamoyl]piperazin-1-yl]-1-oxohexan-2-yl}carbamate; **(4)***

DIPEA (0.27 mL, 1.52 mmol, 2 eq), benzyloxycarbonyl-(Boc)-Lysine (CombiBlock, San Diego, CA, USA) (0.31 g, 0.83 mmol, 1.1 eq) and HATU (0.46 g, 1.22, 1.6 eq) were all dissolved in ACN under nitrogen atmosphere and stirred at room temperature for 15 min. Compound **3** (0.33 g, 0.76 mmol, 1 eq) was then added, and the reaction was stirred at room temperature until completion (4.5 h) (TLC system DCM/MeOH 95/5 + ninhydrin stain, 4.5 h). The ACN was then evaporated, and the resulting crude oil was dissolved in EtOAc (10 mL) and washed with 10% HOAc (3 × 10 mL), brine (1 × 10 mL), saturated $NaHCO_3$ (3 × 10 mL) and brine again (3 × 10 mL) before being dried over anhydrous $MgSO_4$, filtered and concentrated. The resulting crude material was directly dissolved in an excess HCl/dioxane 4 M solution in DCM and the reaction was stirred at room temperature until completion (1 h, TLC system EtOAc/MeOH 95/5 + ninhydrin stain). The HCl/dioxane solution was evaporated and the resulting product was precipitated with cold Et_2O and used directly in the next reaction without further purification (crude yield 85%).

*benzyl N-{1-[(2R)-4-(naphthalene-1-carbonyl)-2-[(prop-2-yn-1-yl)carbamoyl]piperazin-1-yl]-1-oxo-6-(prop-2-enamido)hexan-2-yl}carbamate **(5, AA9p)**.*

Compound **4** (0.08 g, 0.13 mmol, 1 eq) and DIPEA (0.04 mL, 0.26 mmol, 2 eq) were suspended in a mixture of ACN and *t*-butyl alcohol (Fisher Scientific (Ottawa, ON, Canada) (1/1, v/v) followed by the slow addition of acryloyl chloride (0.011 mL, 0.14 mmol, 1.1 eq). The reaction was stirred at room temperature until completion in 30 min (TLC system DCM/MeOH 95/5 + ninhydrin stain, 30 min). The solvents were concentrated and the resulting crude material was dissolved in EtOAc (5 mL) and washed with 10% HOAc (3 × 5 mL), brine (1 × 5 mL), saturated $NaHCO_3$ (3 × 5 mL) and brine again (3 × 5 mL) before being dried over anhydrous $MgSO_4$, filtered and concentrated. Subsequent preparative TLC (DCM/MeOH 95/5) led to final compound **5** (aka **AA9p**) in a 27% yield. The purity of final compound **AA9p** was determined by reverse-phase High Performance Liquid Chromatography (HPLC) to be 100%. ^{1}H-NMR (600 MHz, $CDCl_3$): 1.15–1.32 (1H, m), 1.33-1.49 (2H, m), 1.49-1.59 (1H, m), 1.59-1.98 (1H, m), 2.00-2.35 (1H,m), 2.50-3.09 (1H, m), 3.10-3.47 (3H, m), 3.50-3.69 (1H, m), 3.70-3.94 (1H, m), 3.97-4.10 (1H, m), 4.11-4.32 (1H, m), 4.33-4.56 (1H, m), 4.57-4.82 (1H), 4.88-5.05 (1H, m), 5.06-5.14 (1H, m), 5.105-5.43 (1H, m), 5.49-5.73 (1H, 3 ×

broad s), 5.77-5.89 (1H, broad s), 6.02 (1H, q, *J*=8.89 Hz), 6.18 (1H, m, *J*=9.17 Hz), 6.26 (1H, t, *J*=11.47 Hz), 7.14 (1H, 2 small broad s), 7.31 (4H, q, *J*=8.41 Hz), 7.41-7.77 (4H, m), 7.78-7.91 (2H, m), 7,92-8.40 (1H, 2 × d, *J*= 8.22 Hz), 8.12-8.30 (1H, 2 × s). ^{1}H VT NMR (600 MHz, 50°C, $CDCl_3$): 1.28 (1H, broad s), 1.44 (2H, broad s), 1.56 (2H, broad s), 1.66 (5H, broad s), 2.16 (1H, m), 3.32 (4H, broad s), 4.08 (2H, broad s), 4.56 (1H, broad s), 5.10 (3H, s), 5.57-5.59 (2H, m), 6.05 (1H, m), 6.15 (1H, m), 6.27 (1H, m), 6.93 (1H, broad s), 7.32 (5H, broad s), 7.51 (4H, broad s), 7.88 (3H, broad s). ^{13}C-NMR (151 MHz, $CDCl_3$): HRMS: 15.3, 18.3, 22.2, 29.8, 38.9, 41.6, 46.3, 49.9, 50.9, 55.1, 64.0, 65.9, 67.3, 71.7, 79.3, 102.7, 103.6, 104.2, 124.4, 125.2, 126.1, 126.8, 127.1, 127.5, 128.0, 128.5, 129.5, 130.3, 130.6, 133.4, 135.9, 136.1, 156.2, 157.0, 166.5, 167.3, 168.2, 170.6, 172.3, 172.9. $[M + Na]^+$ calculated = 660.2798, found = 660.2798.

The ^{1}H- and ^{13}C-NMR spectra of **AA9p** both display complex and overlapping splitting patterns that are consistent with the presence of multiple rotamers having distinct interconverting conformations. The limited rotation of the C–N amide bond, as well as the hindered interconversion of the two possible piperazine ring chair conformations, further impacted by the unsymmetrical functionalization of the ring by planar aryl groups (e.g. naphthoyl moiety) have all been described as direct causes for the observation of several (>2) rotamers in *N,N*-dialkylated amide piperazines [22,23]. This phenomenon was observed as soon as the naphthoyl moiety was introduced on compound **3**, giving three distinctive observable rotamers and a clear splitting of the piperazine and propargylic peaks on the ^{1}H-NMR and ^{13}C-NMR spectra. Variable temperature ^{1}H NMR was performed in $CDCl_3$ at 50°C to validate this hypothesis [23,24], showing coalescence of peaks in the expected piperazine proton signals (2.8 - 4.8 ppm) as well the alkene proton region (acrylamide moiety, 5.8 - 6.8 ppm), the aromatic region (7 – 9 ppm), and the methylene region (1 - 1.8 ppm), as shown in Fig. 1B.

2.10.2. Kinetic evaluation of AA9p

Recombinant TG2 was expressed and purified from *E. coli* through either enzymatic cleavage with the Human rhinovirus 3C protease as previously described (for intact mass analysis) or through Ni-nitrilotriacetic acid resin-based elution as recently described (for enzymatic assays) [25].

AA9p was evaluated as an inhibitor to confirm that the additional propargyl amide group, compared to **AA9**, did not affect its inhibitory activity. Using our well-established colorimetric kinetic assay [26], the rate constants for the time-dependent inactivation of TG2 (k_{obs}) were measured under Kitz and Wilson conditions in the presence of varying concentrations of **AA9** and **AA9p**. These rate constants were then fitted to a hyperbolic equation, providing the irreversible inhibition parameters k_{inact} and K_I (Fig. 1C).

2.10.3. Mass spectrometric analysis of the modification of TG2 by AA9p

2.10.3.1. Intact mass analysis. Micro centrifuge tubes were obtained from FroggaBio Inc. (Concord, ON, Canada). Glacial HOAc was obtained from Anachemia Science (Lachine, QC, Canada). Two-mL clear HPLC vials and glass inserts were obtained from Agilent (Santa Clara, CA, USA). Formic acid and Liquid Chromatography–Mass Spectrometry solvents (H2O and ACN) were obtained from Sigma-Aldrich (Saint Louis, MO, USA). Trypsin Gold, Mass Spectrometry Grade was obtained from Promega.

TG2 (2.5 μM) was incubated for 30 min with 5 eq of AA9 (12.5 μM) in a calcium rich buffer (100 mM MOPS, Sigma-Aldrich, 15 mM $CaCl_2$, pH=6.9). The buffer was then exchanged with a 10 mM ammonium bicarbonate solution using Amicon tube centrifugation (Sigma-Aldrich, 10-kDa membrane, 4 cycles) and the protein concentration was re-assessed by Bradford assay (Thermo Fisher Scientific, 0.64 μM). Fifty μL of the protein sample was then transferred into a 0.5 mL micro-centrifuge tube and 4 μL of glacial HOAc was added. After mixing the solution for 30 s by vortexing for 30 s, it was transferred into a clear 2-mL HPLC vial containing a 250-μL glass insert with a polytetrafluoroethylene (PTFE)-lined cap (Agilent). All data were acquired using an Agilent 6546 QToF with an Agilent 1260 LC system with the following source parameters: gas temperature 200°C, drying gas 10 L/min, nebulizer 50 psi, sheath gas temp 300°C, sheath gas flow 12 L/min, VCap 3500 V, fragmentor 150 V, skimmer 75 V, Oct 1 RF Vpp 750 V, mass range of m/z 1000-3200 and an acquisition rate of 3 spectra/s was used for each run. Intact mass analysis was completed using flow-injection analysis through a stainless steel HPLC union, heated to 45°C in the column compartment. Injection volume was set at 5 μL with a flow rate of 0.010 mL/min using H_2O + 0.1% (v/v) formic acid (Sigma-Aldrich) for 6.5 min. The system was then flushed at 0.2 mL/min with 50:50 H_2O:ACN (Sigma-Aldrich) + 0.1% formic acid (v/v) for 1min, followed by a 5 min equilibration period back to initial starting conditions. Raw data extraction was performed using Agilent MassHunter Qualitative 10.0. An averaged mass spectrum for each run was obtained by using the "Range Select" function from 3.6 to 5.2 min and extracting the resulting mass spectrum. The averaged mass spectrum was exported as a text file and imported into UniDec 6.0.4 for spectral deconvolution (Fig. 1D). The data were processed using the "Data Processing" module with the following settings: m/z; 1100-2250, Use Background Subtraction, Subtract Curved; 100, Intensity Threshold; 0.2, Normalize Data, and Nonlinear. After data processing, spectral deconvolution was performed using the "UniDec Parameters" module with the following settings: Charge Range; 30 to 80, Mass Range; 70000 to 100000 Da, Sample Mass Every (Da); 1, Smooth Nearby Points; Some, Suppress Artifacts; None. Additional deconvolution parameters were kept as default.

2.10.3.2. Modified residue identification. The recombinant TG2 used in this assay was expressed and purified as described above. Sixty μg of TG2 was dissolved in 50 μL of 10 mM ammonium bicarbonate and incubated at 70°C for 5 min for protein denaturation. The sample was allowed to cool to room temperature and trypsin (Promega) was then added at 1:20 w/w ratio of the protein and incubated for 18 h at 37°C. The tryptic digest was then transferred to a clear 2-mL HPLC vial containing a 250-μL glass insert with a PTFE-lined cap for liquid chromatography–tandem mass spectrometry (LC-MS/MS) analysis (Agilent). All data were acquired using an Agilent 6546 QToF operated in positive polarity with an Agilent 1260 LC system with the following source parameters: gas temp 280°C, drying gas 10 L/min, nebulizer 50 psi, sheath gas temp 300°C, sheath gas flow 12 L/min, VCap 3500 V, fragmentor 150 V, skimmer 65 V, Oct 1 RF Vpp 750 V. A mass range of m/z 50-1700 and an acquisition rate of 3 spectra/s was used for each run. A data-dependent MS/MS acquisition method with a quadrupole isolation width of 1.3 m/z was used with the following settings: 5 precursors/cycle, absolute threshold 5000 counts, active exclusion enabled after 2 spectra and released after 0.05 min, abundance-dependent accumulation of 25000 counts/spectrum, purity stringency of 100% and a purity cut-off of 30%. The collision energy was set using the formula (Slope)*(m/z)/100 + Offset, where Slope and Offset were set at 5 and -6 for Charge 2, 4.3 and -1.3 for Charge 3, 2 and 10 for Charge >3 and 0 and 27.5 for unknown charge.

HPLC separation was completed using an Agilent Poroshell 120 EC-C18 2.7 μM, 3.0 × 150 mm column, where it was heated to 45°C. The injection volume was set to 10 μL with a flow rate of 0.5 mL/min using H_2O + 0.1% (v/v) formic acid (Sigma-Aldrich) for mobile phase A and ACN + 0.1% (v/v) formic acid (Sigma-Aldrich) for mobile phase B. The following HPLC gradient was used for all analyses: 0 min 1% B, 4 min 1% B, 50 min 100% B, 55 min 100% B. The column was then re-equilibrated for 5 min at the initial starting conditions. Data analysis was performed using Skyline 25.1 [27]. Briefly, the amino acid sequence of TG2 was imported into the Skyline target list to create a suspect list of peptides with AA9 modifications. Peptide settings were set as follows: enzyme, trypsin; max missed cleavages, 0. For modifications, a variable modification with a chemical formula of $C_{32}H_{36}N_4O_5$ to a cysteine was

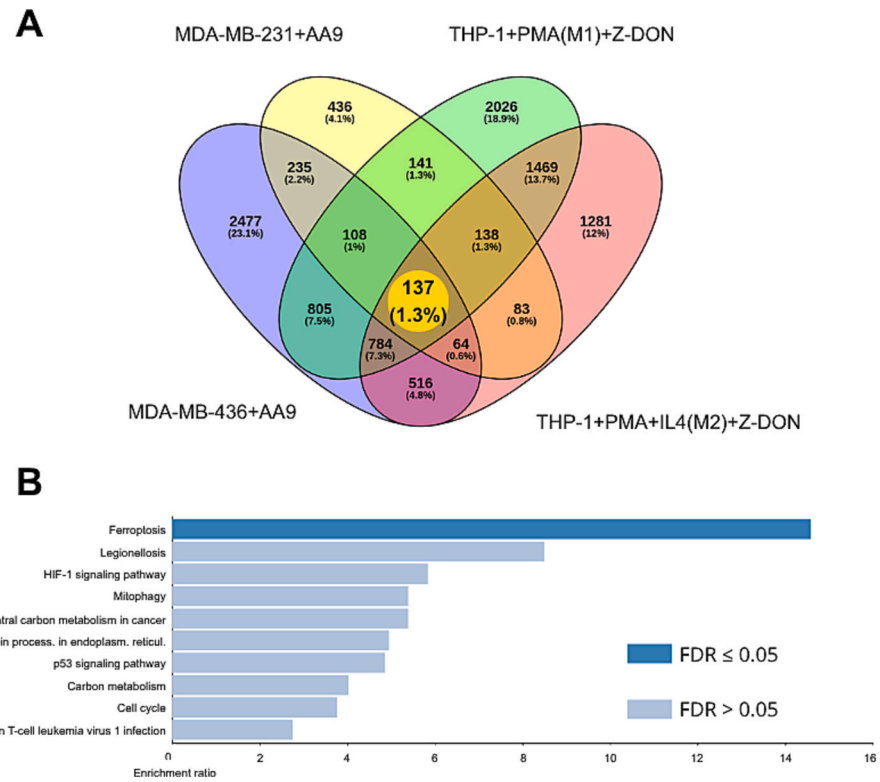

Fig. 2. DEGs and pathway enrichment after treatment with TG2 inhibitor in different models. In A, the Venn plot shows the intersections of DEGs from two different breast cancer cell lines (MDA-MB-231 and MDA-MB-436) treated with the intracellular TG2 inhibitor AA9, and the monocytic THP-1 cell line differentiated toward M1 and M2 macrophage polarizations treated with PMA, Z-DON inhibitor with or without IL-4. In B, the barplot represents the ORA results of common DEGs, using the KEGG pathways list collection. The dark Blue bar depicts FDR ⩽ 0.05; on the contrary, light Blue bars have FDR > 0.05.

added with max variable mods and losses set at 1. Transition settings were set as follows: precursor mass, monoisotopic; product ion mass, monoisotopic; precursor charges, 1-4; ion charges, 1-2; ion types, y and b; ion match tolerance, 10 ppm. From the peptide list, peptides with a green checkmark or yellow triangles were selected for further manual inspection of the MS/MS spectrum (Fig. 1E) to confirm the identification.

2.10.4. In vitro capturing of protein targets using streptavidin/magnetic beads and biotinylated AA9p

We used 9 T-125 flasks (Biosigma, Cona, VE, Italy) of cells harvested at 70-80% confluence, collected at 1200 rpm for 10 min at 4°C, and washed twice with PBS solution. The cells were resuspended in 500 μL buffer (50 mM Tris-HCl pH 7.4, 150 mM NaCl, 1 mM EDTA, and 1× protease inhibitors, Merck KGaA), homogenized by T10 basic ultra-turrax (VWR International, Milan, Italy), and stored 1-2 days at -80°C to further break down. Cell debris was removed by two rounds of centrifugation at 11000 rpm for 20 min at 4°C and the supernatant recovered, obtaining about ~5 μg/μL of proteins. Each assay was performed to detect proteins reacting with an AA9 derivative, AA9p, pendant propargyl group, using as input 15 μg of proteins in a final volume of 250 μL of the buffer reported above. In the first step, we incubated the lysates for 1 h with or without an excess of AA9p at 500 μM of concentration. We exploited its ability to react with biotin-PEG3-azide, for the capturing of the complexes, using streptavidin/magnetic beads. In the second step to bind the AA9p-complexes to biotin, we added 9 μM $CuSO_4$ (Merck KGaA), 18 μM Ascorbate (Merck KGaA), and 180 μM biotin-PEG3-azide (Merck KGaA), and we continued the incubation for 2 h. In the third step, each sample was incubated with 20 μL of streptavidin-magnetic beads (Roche, Monza, Italy, cat. 11641778001) for 30 min at 30°C and washed ten times with 250 μL buffer (50 mM Tris-HCl pH 7.4, 150 mM NaCl, 1 mM EDTA, Merck KGaA). Finally, proteins were recovered in 25 μL of 200 mM 2-mercaptoethanol (Merck KGaA) and 2% sodium dodecyl sulfate (Merck KGaA) by denaturation at 80°C for 10 min, and the beads were separated using a magnetic system. The samples were stored at -80°C until use.

2.10.5. Proteomic analysis of cellular lysates

The reagents used for proteomic sample preparation and LC–MS/MS analysis were all sourced from Merck KGaA, unless specifically indicated.

A concentrated buffer was added to each sample to obtain final concentrations of 1 M guanidinium hydrochloride, 5 mM tris(2-carboxyethyl)phosphine, and 20 mM chloroacetamide in 100 mM Tris-HCl (pH 8.0). Samples were then incubated at 95°C for 10 min under agitation to allow simultaneous protein denaturation, reduction, and alkylation. Proteins were purified according to the protocol described by Koenig *et al.* [24] and subsequently subjected to on-beads digestion with LC–MS grade trypsin (Promega) in 100 mM Tris-HCl (pH 8.0) at 37°C for 16 h. Proteolysis was quenched by adjusting the pH to 2 with 1% TFA; resulting peptides were then purified using Oasis HLB 96-well Plate (3 mg sorbent; Waters, Milford, MA, USA). Eluates were dried in a speedvac and reconstituted in 50 μL of 0.1% Formic Acid prior to LC–MS/MS analysis.

Tryptic peptides were analyzed on a Vanquish Neo nano-HPLC coupled to an Orbitrap Exploris 240 mass spectrometer with a nano-ESI Easy-Spray source (Thermo Fisher Scientific). LC Separation was performed in direct injection mode on a PepMap Neo C18 column (150 mm × 75 μm, 2 μm) at 500 nL/min with a gradient program and total runtime was 30 min. MS scans were acquired at a resolution of 60,000, while MS/MS spectra were collected in data-dependent acquisition mode using a 4 Th isolation window, a resolution of 15,000, a cycle time of 1 s, and a normalized HCD collision energy of 28%.

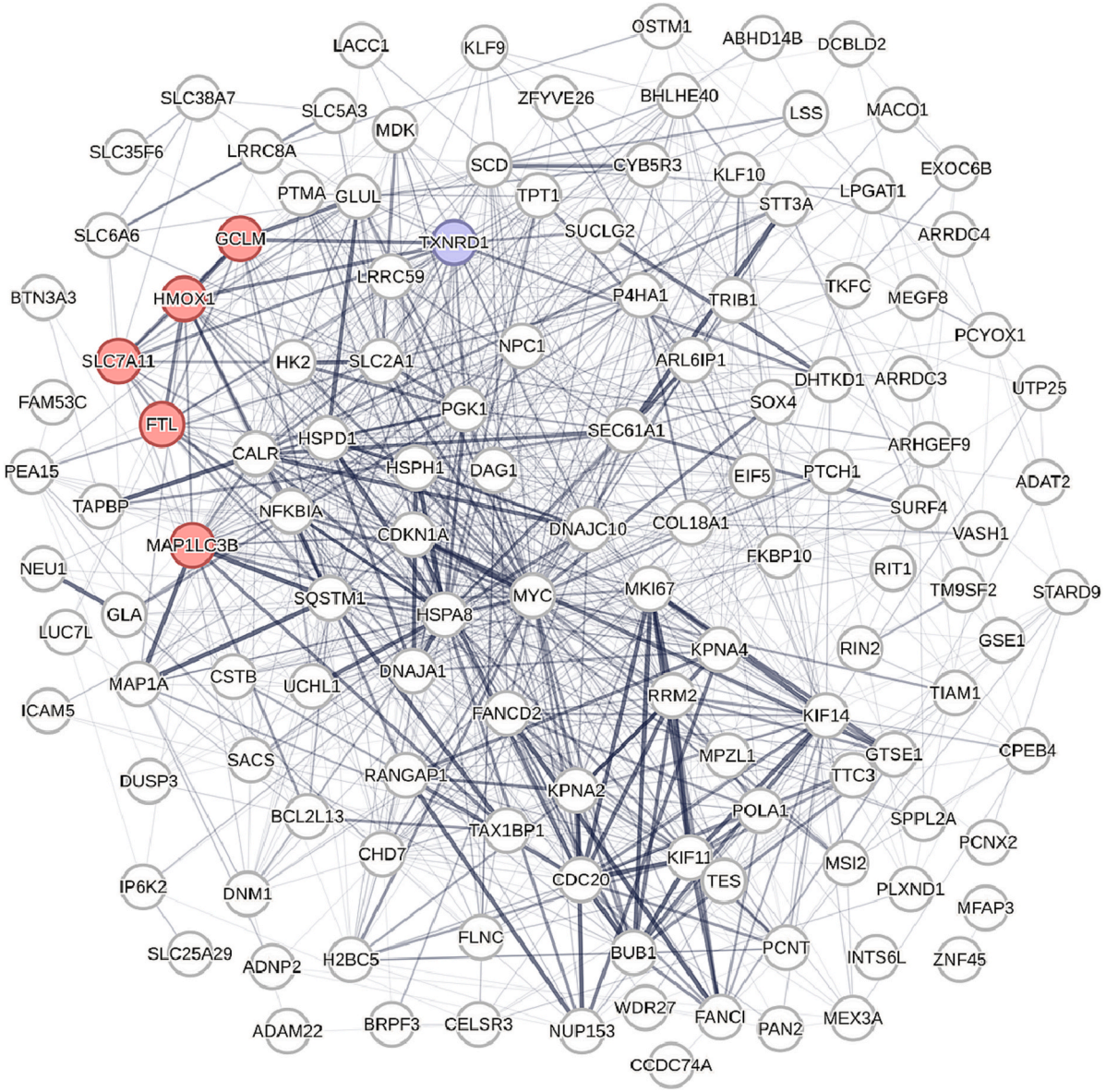

Fig. 3. Network generated by STRING software v.12.0. It has been obtained using the common genes reported in A as input. We set the following parameters: full string networks (the edges indicate both functional and physical protein associations); active interaction sources: text mining, experiment, databases, co-expression, neighbourhood, gene fusion, co-occurrence; interaction score with low confidence; query proteins only, no first shell interactors. Only 129 were included in the network according to the parameters set. The nodes in Red represent genes included in the ferroptosis pathway, according to KEGG and Wiki-pathway gene collections, while in light Blue the gene included only in Wikipathway's ferroptosis pathway collection. Network edges depict the confidence of the connections, where the line thickness indicates the strength of data support.

2.10.6. Bioinformatics and statistical analysis

The raw files were processed using Fragpipe v. 23.0 [28] searching against a library generated from the Swiss-Prot Human proteome database (https://www.uniprot.org/, last access 20/06/2025), supplemented with common contaminants. Downstream analysis was conducted using Perseus Software v2.1.5 [29], following the approach described by Reinisch *et al.* [30]. Contaminant proteins and those with a protein-level Q-value > 0.05 were excluded.

Proteins showing a Fold Change $\geqslant 9$ were included in the functional analysis, performed using the clusterProfiler package in R, with KEGG as the pathway reference database. Resulting pathways were then filtered based on adjusted p-values (Benjamini–Hochberg correction). Visualization of the significantly enriched pathways was performed using the pathview package. Finally, protein–protein interaction networks were obtained using STRING v12.0 (https://string-db.org/, accessed on 13 December 2025), with the following parameters: experimentally validated physical interactions only; interaction score threshold of 0.150 (confidence); number of first-shell interactors limited to a maximum of five.

3. Results

3.1. Treatment with TG2 inhibitors points out ferroptosis as a consensus pathway

To investigate whether the inhibition of TG2 by different compounds modulates shared molecular pathways across samples of distinct origins, we analyzed RNA-sequencing datasets available in the GEO (https://www.ncbi.nlm.nih.gov/gds, accessed on 27 October 2025). The first dataset, GSE222284, contains human transcriptomes from monocytic leukemia cells differentiated into M1 macrophages or polarized into M2 macrophages, either controls or treated with the irreversible

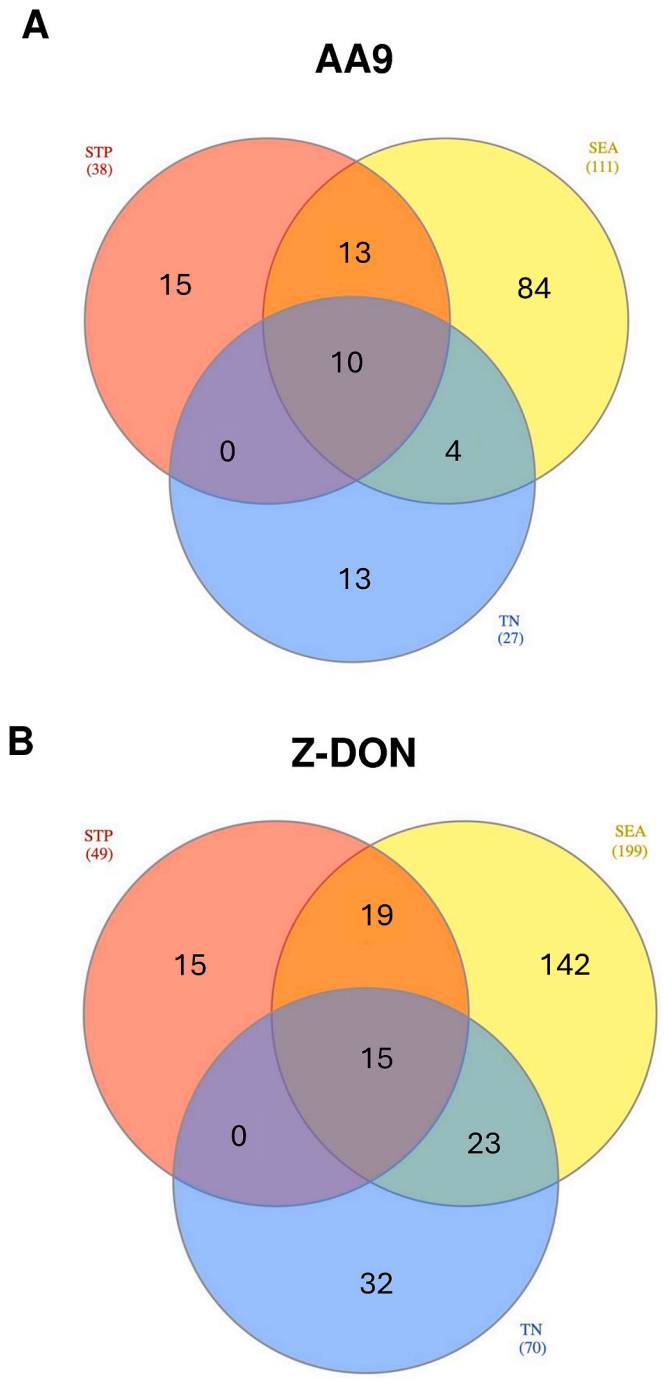

Fig. 4. Venn diagram of the potential cellular targets of TG2 inhibitors, as identified by STP, SEA, and TN. In A, predicted targets interacting with AA9. The 10 proteins identified in the central intersectional area, including TG2, are listed in Table 2. In B, predicted targets interacting with Z-DON.

cell-permeable TG2 inhibitor Z-DON [14]; the second dataset includes RNA profiles from MDA-MB-436 and MDA-MB-231 breast cancer cell lines, stimulated or not with AA9, another irreversible TG2 inhibitor [10]. All considered datasets were generated using comparable procedures: mRNA enrichment with oligo(dT) beads, rRNA removal, cDNA library preparation, and Illumina-based sequencing, allowing a collective comparison.

A Venn diagram was constructed to visualize the intersection of genes commonly deregulated (Fig. 2A). We detected 137 genes (~1.3% of total), which were subsequently subjected to ORA identifying ferroptosis (KEGG: hsa04216) as the only pathway significantly enriched upon TG2 inhibition, with an enrichment factor of nearly 15-fold using FDR ⩽ 0.05 (Fig. 2B).

Table 2
Predicted targets of AA9, according to STP, SEA, and TN.

Gene symbol	UniProt	Name protein	Enriched using AA9p
TGM2	P21980	Protein-glutamine gamma-glutamyltransferase 2	Yes
HDAC1	Q13547	Histone deacetylase 1	Yes
CAPNS1	P07384	Calpain-1 catalytic subunit	No
CTSL	P07711	Cathepsin L	No
CTSB	P07858	Cathepsin B	No
F7	P00734	Prothrombin	No
SIRT2	Q8IXJ6	NAD-dependent protein deacetylase sirtuin-2	No
SIRT1	Q96EB6	NAD-dependent protein deacetylase sirtuin-1	No
HDAC6	Q9UBN7	Protein deacetylase 6	No
TPSAB1	Q15661	Tryptase alpha/beta-1	No

We employed STRING software v.12.0 (https://string-db.org, accessed on 30 October 2025) to investigate potential interactions among these deregulated genes, of which only 129 met the STRING's interaction criteria. The resulting network from KEGG and WikiPathways collections highlights as ferroptosis-associated genes *HMOX1*, *FTL* (Ferritin light chain), *SLC7A11*, *GCLM* (Glutamate-Cysteine Ligase Modifier Subunit), *MAP1LC3B* (Microtubule-associated proteins 1A/1B light chain 3B), and *TXNRD1* (Thioredoxin Reductase 1) (Fig. 3).

Although several studies have investigated the biological consequences of TG2 depletion using genetic approaches such as siRNA or CRISPR/Cas9-mediated knockout, their integration with transcriptomic profiling remains limited. To further explore whether TG2-dependent transcriptional programs are conserved across different tumour contexts, we interrogated a publicly available dataset derived from colorectal carcinoma (CRC) cell lines in which *TGM2* was genetically ablated using shRNA or CRISPR/Cas9 approaches [31]. By integrating datasets from SW480 and HCT116 cells with our RNA-sequencing data obtained from breast cancer cell lines, we further identified 28 significantly deregulated genes shared across these distinct models (link: https://docs.google.com/spreadsheets/d/1HB6_lzffQ7JuZO56wOqC2wg1Q11eH4uP/edit?gid=591178601#gid=591178601). ORA of this common gene set revealed ferroptosis as the top enriched pathway (combined score = 255.68), further supporting a conserved link between TG2 inhibition and ferroptosis-related transcriptional programs across different cellular models. Among the shared genes, particular attention was drawn to *MAP1LC3B* and *HMOX1*, both of which are well-established regulators of cellular stress responses and ferroptosis-associated processes.

3.2. Bioinformatic prediction of AA9 and Z-DON targets

In an effort to predict the selectivity and putative targets of AA9 and Z-DON inhibitors, we adopted a bioinformatic approach using three different web-based screening tools [32]. Swiss Target Prediction (STP) (http://www.swisstargetprediction.ch, accessed on 7 December 2025) employs the 2D and 3D similarity between the ligand of interest and a library of 370000 ligands known to bind > 3000 proteins to predict the targets [33]. The Similarity Ensemble Approach (SEA) (https://sea.bkslab.org, accessed on 7 December 2025) uses the structural similarity of a test ligand with known ligands to predict which proteins may bind the test ligand [34]. TargetNet (TN) evaluates a test ligand against QSAR models for 623 human proteins to predict which ones may bind the ligand of interest [35].

When AA9 was analyzed, STP returned the highest probability for binding TG2, with 37 other proteins providing lower but non-zero probability. SEA also predicted TG2 as the highest probable target, along with 110 other proteins with non-zero probability, and TN

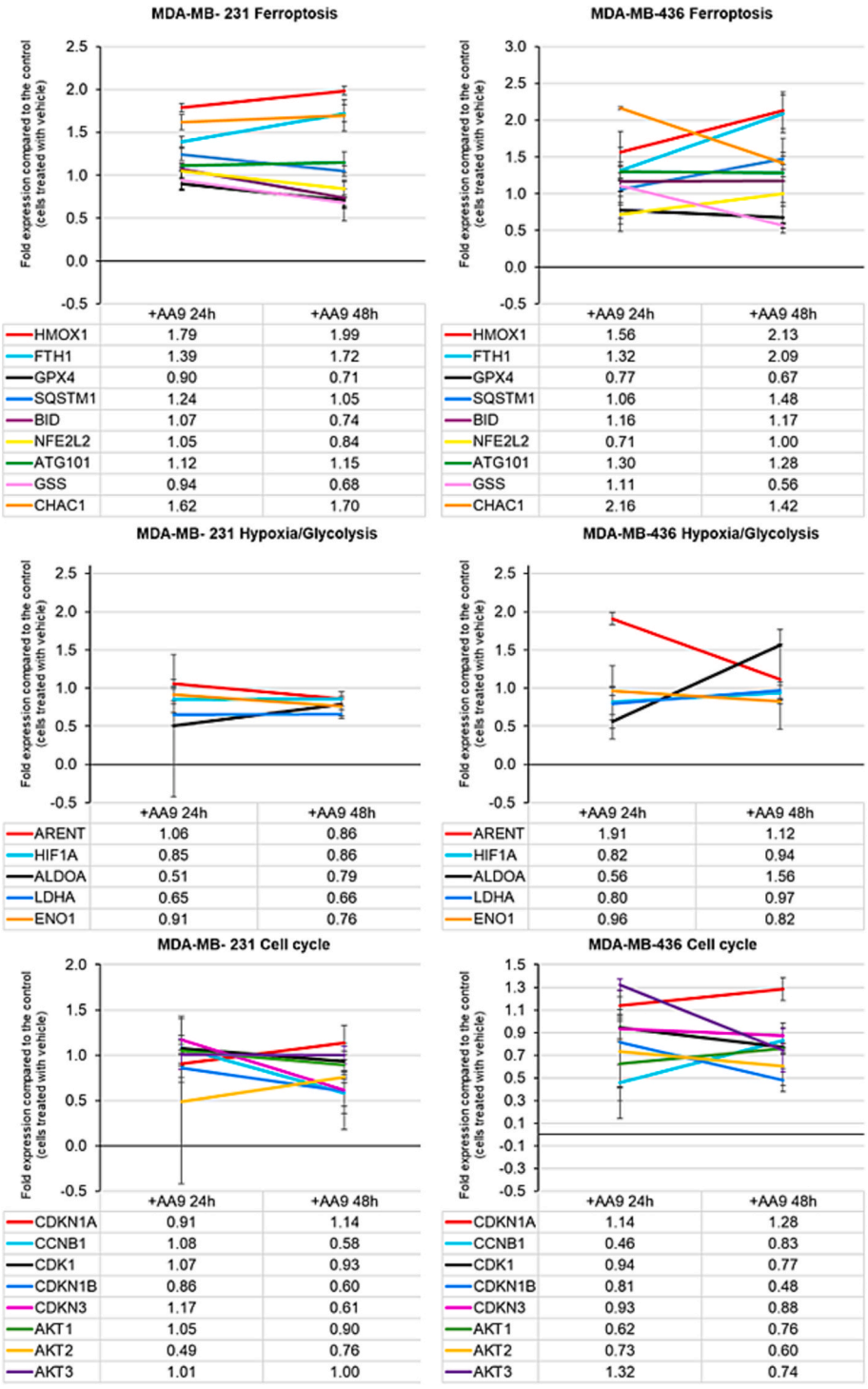

Fig. 5. Expression of genes involved in ferroptosis induced by AA9. Left panel, MDA-MB-231 and right panel, MDA-MB-436 cells were treated with 50 μM AA9 or 0.1% DMSO as the vehicle for 24 h and 48 h. RT-qPCRs were carried out on 1 μg of total RNA. Data derived from n = 3 independent experiments. For quantitative PCR normalization, the median expression of *GAPDH* and *ACTB* was used as reference, and the Fold Change of each sample was calculated using the $2^{-\Delta\Delta CT}$ formula and the samples treated with the vehicle as control. The mean ± standard deviation (SD) was graphed. The deregulation of the following targets was statistically significant: *HMOX1, FTH1, CHAC1, GPX4, GSS, ALDOA, LDHA, CCNB1, CDKN1B, CDKN3, AKT2*, (*$p < 0.05$, using a two-tailed Student's *t*-test).

identified TG2 as the most likely target, along with 26 other proteins whose probability ranged down to 0.08. A Venn diagram was constructed from these three independent predictions, using the online tool known as InteractiVenn (http://www.interactivenn.net, accessed on 7 December 2025) [36]. This analysis, shown in Fig. 4A, identified 10 possible target proteins using all three web tools (Table 2). Thus, TG2 was the top target predicted by all methods.

When Z-DON was subjected to the same evaluation, STP predicted 49 possible targets, including TG2 among the highest ranked. SEA identified 199 potential human proteins and ranked TG2 as the most probable. TN predicted 70 total proteins with a score over 0.08, but not TG2, nor any other TGase. Therefore, TG2 was not found in the intersectional area of the Venn diagram shown in Fig. 4B. Notably, the 15 proteins at this intersection, predicted by all three web tools, were all amidases and

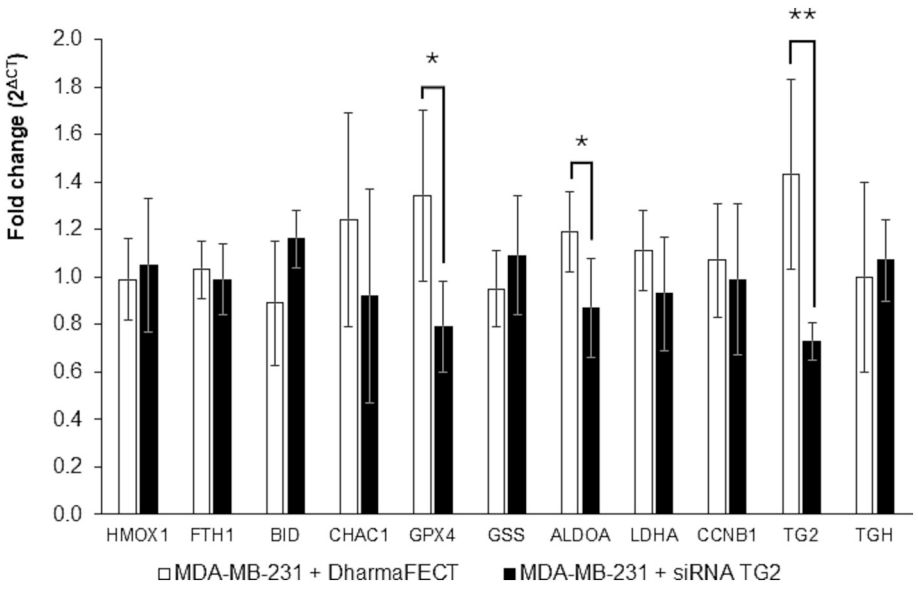

Fig. 6. TG2 silencing modulates ferroptosis- and metabolism-related gene expression in MDA-MB-231 cells. Relative mRNA levels of the indicated genes, assessed by RT-qPCR in cells transfected with control reagent (DharmaFECT) or TG2-specific siRNA. For quantitative PCR normalization, the geometric median of the expression *GAPDH* and *ACTB* were used, and the Fold Change of each sample was calculated using the $2^{-\Delta CT}$ formula. Data are presented as mean ± SD of four independent experiments. *Statistical significance was determined using a two-tailed unpaired Student's *t*-test assuming equal variances (*$P < 0.05$; **$P < 0.01$).

proteases (Plasminogen, Urokinase-type plasminogen activator, Calpain 1, Trypsin I, Cathepsin L, Cathepsin B, Cathepsin K, Leukocyte elastase, Chymase, Caspase 1, Caspase 3, Endothelin-converting enzyme 1, Prolyl endopeptidase, Caspase 8, Tryptase β1), which is understandable, given the peptidic structure of Z-DON.

In conclusion, we selected AA9 in our further investigations, because it recognizes TG2 as the top target across all platforms.

3.3. Beyond ferroptosis, inhibition of TG2 by AA9 modulates metabolic asset and cell cycle in breast cancer

We focused on breast cancer, using TNBC cell lines as a model, given that this subtype still presents significant therapeutic challenges [37]. We performed treatments with AA9 for 24 and 48 h and analyzed the expression of key genes closely associated with ferroptosis, and other

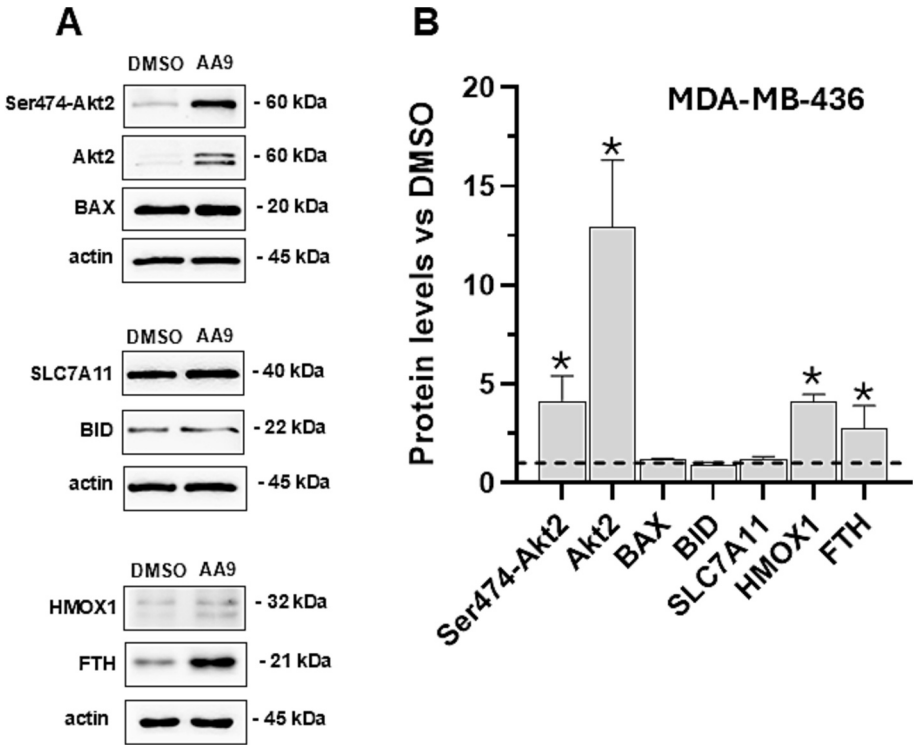

Fig. 7. AA9-dependent regulation of ferroptosis-related proteins in MDA-MB-436 cells. (A) Representative Western blot analysis of cell lysates treated with AA9 for 48 h, using the indicated antibodies. Actin was used as internal control for equivalence of loaded proteins. (B) Quantification of protein levels based on densitometric analysis of Western blot bands, normalized to actin. Data represent the mean ± SD from three independent experiments. *$P < 0.05$ compared to the control conditions taken as 1.

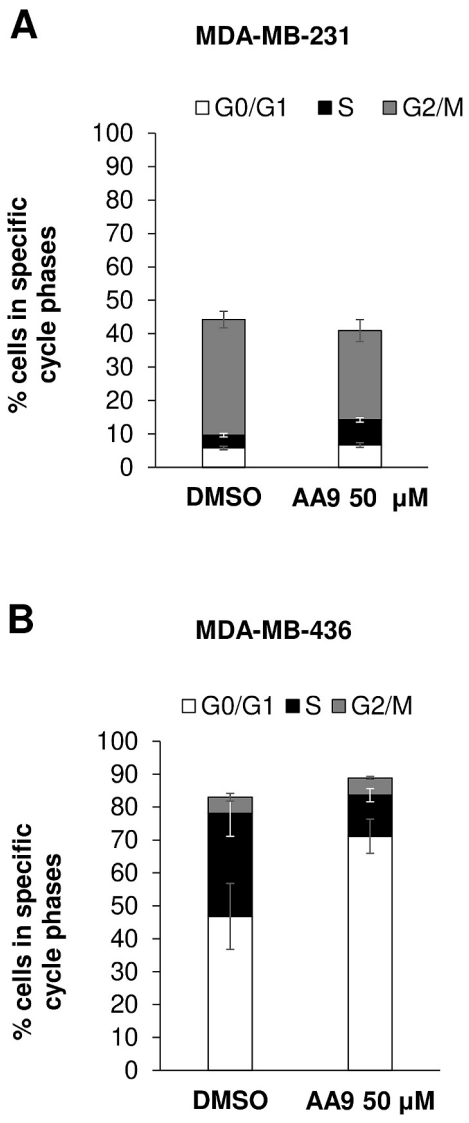

Fig. 8. Inhibition of cell cycle by AA9. (A) MDA-MB-231 and (B) MDA-MB-436 cells were treated with 50 μM AA9 and the vehicle, and cell cycle evaluated using Muse™ Cell Cycle Reagent. The different phases were indicated in the legend. All the data are represented as mean of three independent experiments; bars represent mean ± SD. Student's paired *t*-test of 3 independent experiments using two-tailed: *P* value = 0.01 comparing the percentage of phase S of AA9 to the vehicle, and *P* = 0.015 comparing the percentage of phase G2/M of AA9 to the vehicle.

potentially involved in related signalling pathways and mechanisms. According to literature [38], we selected the following genes: *HMOX1*, *FTH1*, *GPX4*, *SQSTM1* (Sequestosome 1), *BID*, *NFE2L2* (Nuclear factor, erythroid 2-like 2), *ATG101* (Autophagy Related 101), *GSS* (Glutathione synthetase), and *CHAC1* (Glutathione-specific gamma-glutamylcyclotransferase 1) as targets. Concerning additional genes associated with ferroptosis and modulated by hypoxia and related to the Warburg effect [13], we included *HIF1A*, *ARNT* (Aryl Hydrocarbon Receptor Nuclear Translocator), *ALDOA* (Aldolase A), *LDHA* (Lactate dehydrogenase A), and *ENO1* (Enolase 1). As ROS accumulation leads to a slowing of the cell cycle [39], we also analyzed the expression of *CDK1* (Cyclin-dependent kinase 1), *CDKN1A* (cyclin dependent kinase inhibitor 1A), *CDKN1B* (cyclin dependent kinase inhibitor 1B), *CDKN3* (Cyclin-dependent kinase inhibitor 3), *CCNB1* (Cyclin B1), *AKT1*, *AKT2*, and *AKT3*.

Gene expression was quantified by RT-qPCR (reverse transcription quantitative polymerase chain reaction) in MDA-MB-231 and MDA-MB-436 cells, control or treated with AA9, choosing a threshold of about ± 25%. In MDA-MB-231, among the genes closely related to ferroptotic cellular processes, we found upregulated by AA9 *HMOX1*, *FTH1*, *BID*, and *CHAC1*, while *GPX4* and *GSS* were downregulated along with *ALDOA* and *LDHA*, predominantly associated with hypoxia and the Warburg effect; finally, we observed decreased levels of *CCNB1* and *CDKN1B*, mainly linked to cell cycle, after 48 h of treatment (Fig. 5, left panel). In AA9-treated MDA-MB-436 cells, the levels of *HMOX1*, *FTH1, CHAC1,* and *CDKN1A* transcripts similarly increased, and *GPX4, GSS, LDHA,* and *CDKN1B* decreased. In contrast, in this cell line, *ALDOA* reversed the trend at 48 h after treatment (Fig. 5, right panel).

To assess whether these transcriptional changes were directly dependent on TG2, we performed TG2 silencing experiments using a custom siRNA specific for the full-length TG2 and DharmaFECT™ Transfection system, specially developed to transfect particularly difficult cells such as MDA-MB-231. Analyzing the expression of several genes, as shown in Fig. 6, TG2 knockdown partially recapitulated the effects induced by AA9, leading to significant modulation of *ALDOA* and *GPX4* expression, which drove their downregulation. This supports a TG2-dependent regulation of the ferroptotic pathway triggered by altered metabolic remodeling, which underlies redox imbalance.

Consistent with the transcriptional data, Western blot analysis confirmed that AA9 treatment increased HMOX1 and FTH protein levels in MDA-MB-436 cells (Fig. 7), indicating that TG2 inhibition engages stress-responsive iron-handling pathways associated with ferroptosis activation. AA9 treatment increased AKT2 phosphorylation at Ser474, a modification associated with mTORC2-dependent full activation of AKT2 and indicative of engagement of signalling pathways involved in metabolic regulation and cell survival.

The impact on cell proliferation was verified using the Muse™ Cell Cycle Reagent and data analysed by the Muse™ Cell Analyzer. Fig. 8A shows a statistically significant accumulation of cells in S phase and a decrease in the G2/M phase of MDA-MB-231, whereas MDA-MB-436 cells appeared preferentially blocked in G0/G1 phase (Fig. 8B). This indicates that AA9 also affects cell cycle progression and cell growth.

In addition, possible alteration of metabolic status following treatment was assessed by measuring both intra- and extracellular ATP levels in lysates and supernatants of MDA-MB-436 cells, control or exposed to 50 μM AA9 (Fig. 9). After 8 h from AA9 addition, intracellular ATP levels were high and decreased at 24 h, simultaneously with an extracellular increase. The cell-impermeable TG2 inhibitor NCEG2 [40], used as a negative control, did not affect ATP levels when administered at the same concentration.

3.4. *Identification of proteins interacting with AA9 in vitro*

The covalent modification of TG2 with AA9 has been shown to correspond to its time-dependent loss of active site activity [40]. TG2 contains 20 different cysteine residues, 3 of which are involved in an oxidative triad (C370, C371, and C230) responsible for the inactivation/activation of TG2 under different redox conditions [41]. Herein, we confirm that even an excess of AA9 leads to a single modification event, consistent with selective active site alkylation (Fig. 1D). LC–MS/MS analysis of the tryptic digest yielded a single peptide, YGQC(AA9)WVFAAVACTVLR (residues 274-289), that corresponded to being covalently modified by AA9. Further inspection of the MS/MS spectrum of the triply charged precursor (*m/z* 781.7213) revealed a continuous series of y fragment ions from y1 to y12 (Fig. 1E). The presence of this extensive y-ion series localizes the AA9 modification to the cysteine residue at position 277. In addition, two AA9-specific diagnostic ions were observed, providing further confirmation of AA9 modification on the peptide (Fig.1E). Taken together, the complete y-ion coverage and the presence of AA9-specific diagnostic ions demonstrate that the AA9 modification is localized to C277 on TG2.

To determine whether TG2 present in cellular lysates interacts with

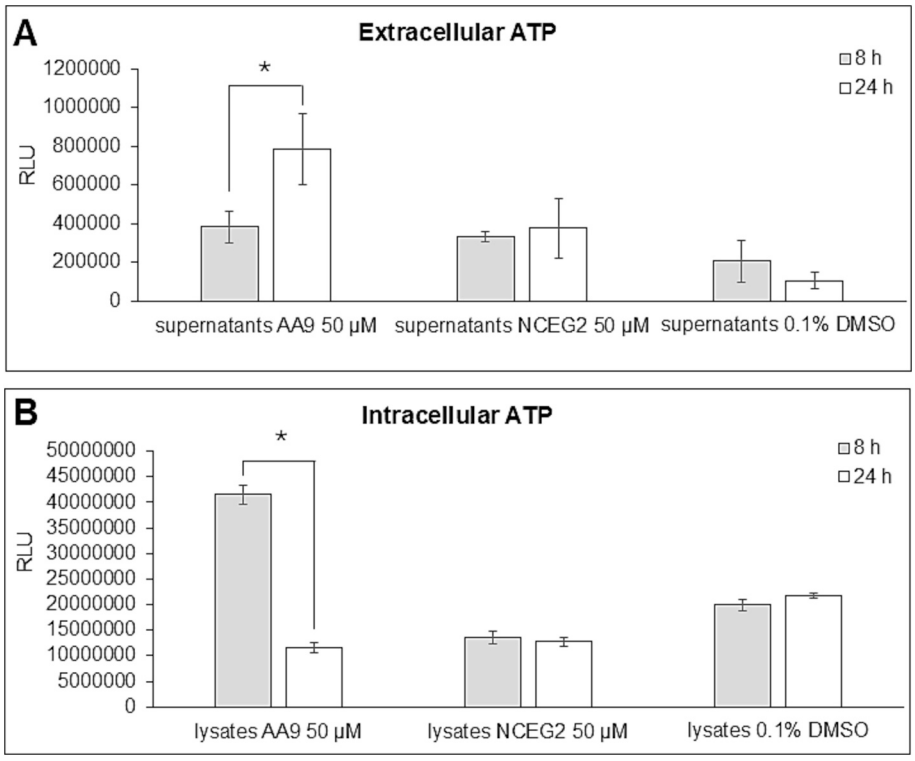

Fig. 9. Changes in ATP levels after treatment with AA9 of MDA-MB-436 cells. (A) Extracellular content of ATP. (B) Intracellular content of ATP. Cells were treated with 50 µM AA9 or 0.5% DMSO, the vehicle, for 8 h and 24 h. Also, lysates and supernatants were analysed using CellTiter-Glo® Reagent per assay in a 96-well format (Promega). The assay was carried out following the manufacturer's protocol and detected using GloMax® Discover (Promega). The mean ± SD from n = 3 independent experiments was graphed, and statistical significance was assessed using two-tailed Student's *t*-test (*$p < 0.05$). The mean ± SD was reported, and statistical significance was calculated using a two-tailed Student's *t*-test (*$p < 0.05$).

AA9, and to identify potential additional binding partners, we performed experiments using MDA-MB-231 cells, whose lower endogenous TG2 levels [11] might facilitate the capture of a higher proportion of potential complexes. Since avidin-biotin technology offers an effective approach for capturing proteins associated with a conjugated molecule [42], we developed an *in vitro* capture system using an AA9 analogue, AA9p. This compound was designed to present a propargyl group on its piperazine core (see Scheme 1), which would allow for bioorthogonal reaction with an azide group, in the *in situ* formation of a triazole linker. Kinetic analysis of AA9p confirmed that its additional propargyl group does not affect the inhibition reaction in any way (see Fig. 1C). However, this propargyl group can undergo crosslinking with azido-biotin, which allows for subsequent isolation with streptavidin-coated magnetic beads (Fig. 10). This approach is conceptually similar to that demonstrated by Hauser *et al.*, who used a biotinylated version of a TG2 inhibitor in an ELISA-based assay to quantitatively measure the engagement of target TG2 in cell lysate [43] and conceptually aligned with activity-based protein profiling approaches [44]. Our method allowed us to confirm the binding of AA9p to TG2 in a cellular environment, and to identify proteins in complex with TG2, in addition to potential off targets of AA9. The isolated complexes were analysed by proteomics, revealing 1598 total proteins, 130 reactive exclusively with AA9p. Among these, TG2 exhibited a high score with a Fold Change > 9.0 (link:https://docs.google.com/spreadsheets/d/1C6xzq3q8WHAeUmNx6hG5sUyPTFQKFOyt/edit?usp=-drive_link&ouid=112878060347254043013&rtpof=true&sd=true). TG2 recovery in the pool of proteins was confirmed by Western blot analysis in two independent experiments (Fig. 10, at the bottom).

The whole list of proteins characterized by proteomics engaged by TG2 and isolated with "AA9-fishing" experiments was subjected to an ORA to investigate their functional enrichment. Using the *clusterProfiler* package in R and KEGG as the pathway collection database, several significantly enriched pathways were identified (adjusted *p*-values < 0.05, Benjamini Hochberg correction). Visualization of the significantly enriched pathways was performed using the *pathview* package, allowing detailed inspection of the molecular components involved. For each pathway, we generated protein–protein interaction networks using STRING v12.0 (https://string-db.org/, accessed on 13 December 2025), focusing exclusively on experimentally validated physical interactions. The resulting interactomes were constructed using confidence-based edges, with thickness proportional to the strength of the supporting evidence. An interaction score threshold of 0.150 (confidence) was applied, and the number of first-shell interactors was limited to a maximum of five, yielding refined and biologically meaningful networks.

From a functional point of view, we found 62 ORA subcategories with FDR ⩽ 0.05 (link: https://docs.google.com/spreadsheets/d/1C6xzq3q8WHAeUmNx6hG5sUyPTFQKFOyt/edit?usp=sharing&ouid=112878060347254043013&rtpof=true&sd=true) notably, those displaying the highest Fold Enrichment were associated with molecular chaperones, such as proteasome with regulatory particles, DNA replication with increase of minichromosome maintenance protein complexes, nucleocytoplasmic transport, and pathways associated with mRNA surveillance/degradation, or protein export mechanism in which the accumulation regarded signal recognition particle and ribosome. In addition, we found cytoskeletal proteins, actin, tubulin, and vimentin belonging to the enriched "regulation cytoskeleton network", through which TG2 establishes an interaction with paxillin at focal adhesions (Fig. 11), and interferes with the pathways of "regulation of actin cytoskeleton" (Fig. 12) and molecular motors. Accordingly to gene expression data, the networks of HIF-1 (Fig. 13A) and glycolysis (Fig. 13B) appeared enriched, with TG2 showing prominent interactions with ALDOA. Finally, other cellular pathways, such as the cell cycle (Fig. 14) and apoptosis (Fig. 15), have also been confirmed. Many of

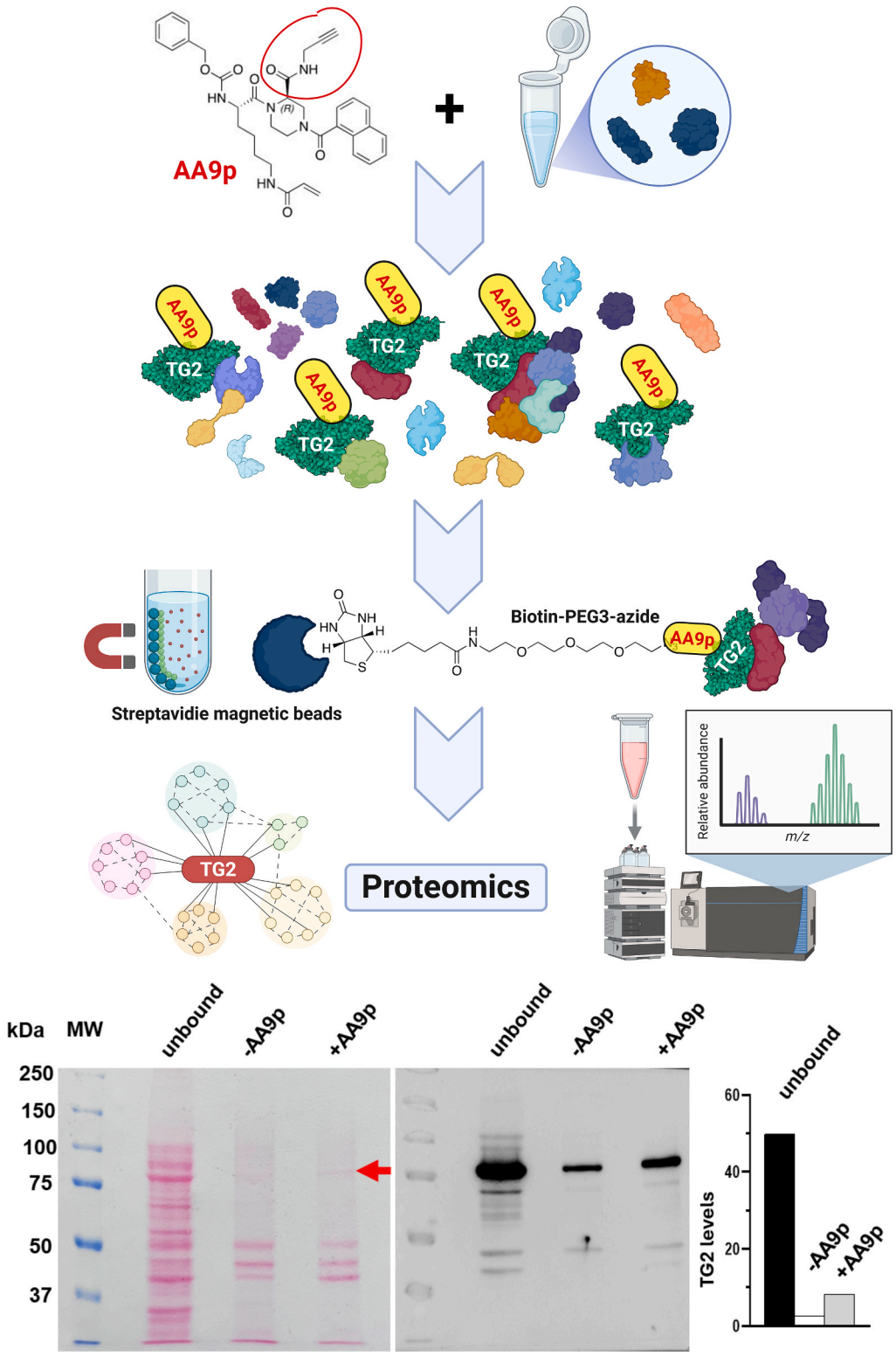

Fig. 10. Capture of target proteins by AA9. Chemical proteomics workflow to identify TG2-interacting proteins using an activity-based probe. The alkyne-functionalized probe AA9p, derived from the parent compound AA9, was used to label TG2 and associated single proteins or complexes in cell lysates of MDA-MB-231 cells. Following incubation, probe-labelled proteins were linked to biotin–PEG3–azide. Biotinylated proteins were enriched using streptavidin-coated magnetic beads and subsequently analyzed by LC-MS/MS. Representative enrichment is shown in the lower panel. Representative Ponceau S-stained nitrocellulose membrane (left) and immunoblots (middle) of TG2 from MDA-MB-231 cells in control condition (unbound), fished with only biotin-PEG3-azide (−AA9p) or after reaction with biotin-PEG3-azide (+AA9p). Total lysates (15 μg protein) were separated on 8.5% denaturing polyacrylamide gels, blotted to nitrocellulose membranes and reacted with anti-TG2 primary antibody (cat. Ig036, Zedira), following the manufacturer's instructions. Membranes were then incubated with peroxidase-conjugated secondary antibodies and revealed with the ECL system. To correctly identify the position of TG2 band, we loaded the molecular weight marker Precision Plus Protein™ All Blue Prestained Protein Standards. Histograms (right) report the levels of TG2 in different experimental conditions as deduced from the densitometry of bands.

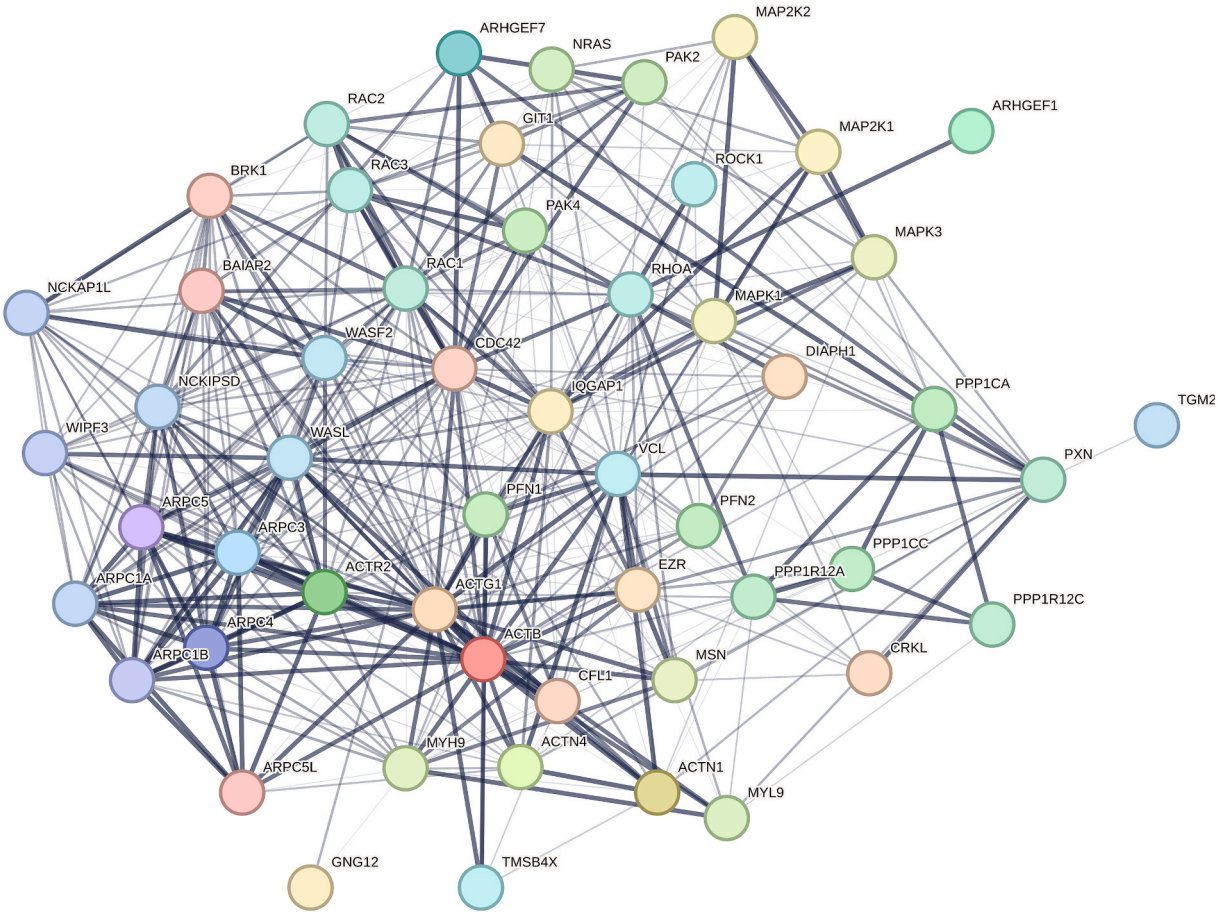

Fig. 11. Proteins target of AA9p interacting physically with TG2 and included in the regulation cytoskeleton network.

these targets (533 proteins) were also detected in an AA9p "fishing" experiment using MDA-MB-436 cells. Consistently, several of the 533 proteins shared between datasets map onto the KEGG pathways identified by ORA, including the proteasome (PSMA/PSMB/PSMC/PSMD family members (hsa03050), RNA processing and spliceosome pathways (Heterogeneous nuclear ribonucleoproteins, HNRNP; Serine/Arginine-Rich Splicing Factor, SRSF; Splicing Factor 3, SF3, and DEAD-box helicase proteins; hsa03040, hsa03018), glycolysis and central carbon metabolism (ALDOA, Pyruvate Kinase M, GAPDH, ENO1, and LDHA; hsa00010, hsa00020), cell cycle and DNA replication (CDK1, Minichromosome Maintenance Complex Components 2–7, and Proliferating Cell Nuclear Antigen; hsa04110, hsa03030), apoptosis and stress-related signalling (BAX, Fas-associated protein with death domain, SQSTM1; hsa04210, hsa04144), and cytoskeleton and focal adhesion pathways (ACTB, Filamin A, Paxillin, and Talin 1; hsa04510, hsa04810).

3.5. *Molecular interaction of TG2 with critical players in ferroptosis and apoptosis*

Considering the deregulation of *HMOX1*, *FTH1*, *CHAC1*, *GPX4*, and *GSS* genes, which suggests ferroptosis activation following TG2 inhibition in AA9-exposed cells, we explored a possible interaction between TG2 and proteins involved in ferroptosis, a distinct form of cell death from the programmed nature of apoptosis. Nevertheless, severe oxidative stress, accumulation of lipid radicals, and mitochondrial dysfunction can elicit secondary apoptotic signalling, as confirmed by interactome analysis.

In MDA-MB-436 breast cancer cells, exhibiting high TG2 expression [11], we investigated the potential association between TG2 and proteins linked to both ferroptosis and apoptosis, BID [45], and BAX [46], respectively. The latter is a pro-apoptotic key mediator demonstrated to interact with the BH3 motif of TG2 in SK-n-BE(2) cells in a way strongly associated with cell death [20]. Rodolfo *et al.* used molecular docking to explore the interaction between TG2 and BAX using various potential ligands, inhibitors, and mutants in the BH3 motive of TG2. They argued that the inhibition of this molecular interaction may induce apoptosis. In fact, TG2 inhibitors, NC9 and AA9, induced apoptosis in MDA-MB-231 and MDA-MB-436 cells [47].

Prompted by these results, we investigated the *in silico* potential association of TG2 with these partners. Docking analysis using HADDOCK confirmed the interaction with BAX (Fig. 16A), and a similar score resulted for its interaction with BID (Fig. 16B). All parameters of these analyses are reported in Table 3. Considering both the open and closed conformation of TG2, the HADDOCK scores of the TG2-BID interaction were more favourable for the closed conformation, suggesting that it may be preferred for the binding of the partner, although the cluster sizes of the open conformations were larger than those of their closed counterparts, suggesting greater flexibility or variability in the interactions. The Root Mean Square Deviation values also suggested lower flexibility in the closed state, as well as Van der Waals Energy being more favourable in the open state, which was consistent with the Restraints Violation Energy values. Additionally, Electrostatic Energy would allow for better alignment with the ligands, potentially due to stronger charge-dipole or ionic interactions. Inversely, the TG2-BAX interaction preferred the open form with a narrower cluster size. Furthermore, desolvation energies were generally lower for the open conformation of TG2 (the lowest value for open TG2-BAX), indicating that in the open form, binding with the ligands caused a lower 'penalty' for surface desolvation, which may favour the formation of a stable complex. On the other hand, based on Buried Surface Area, the closed

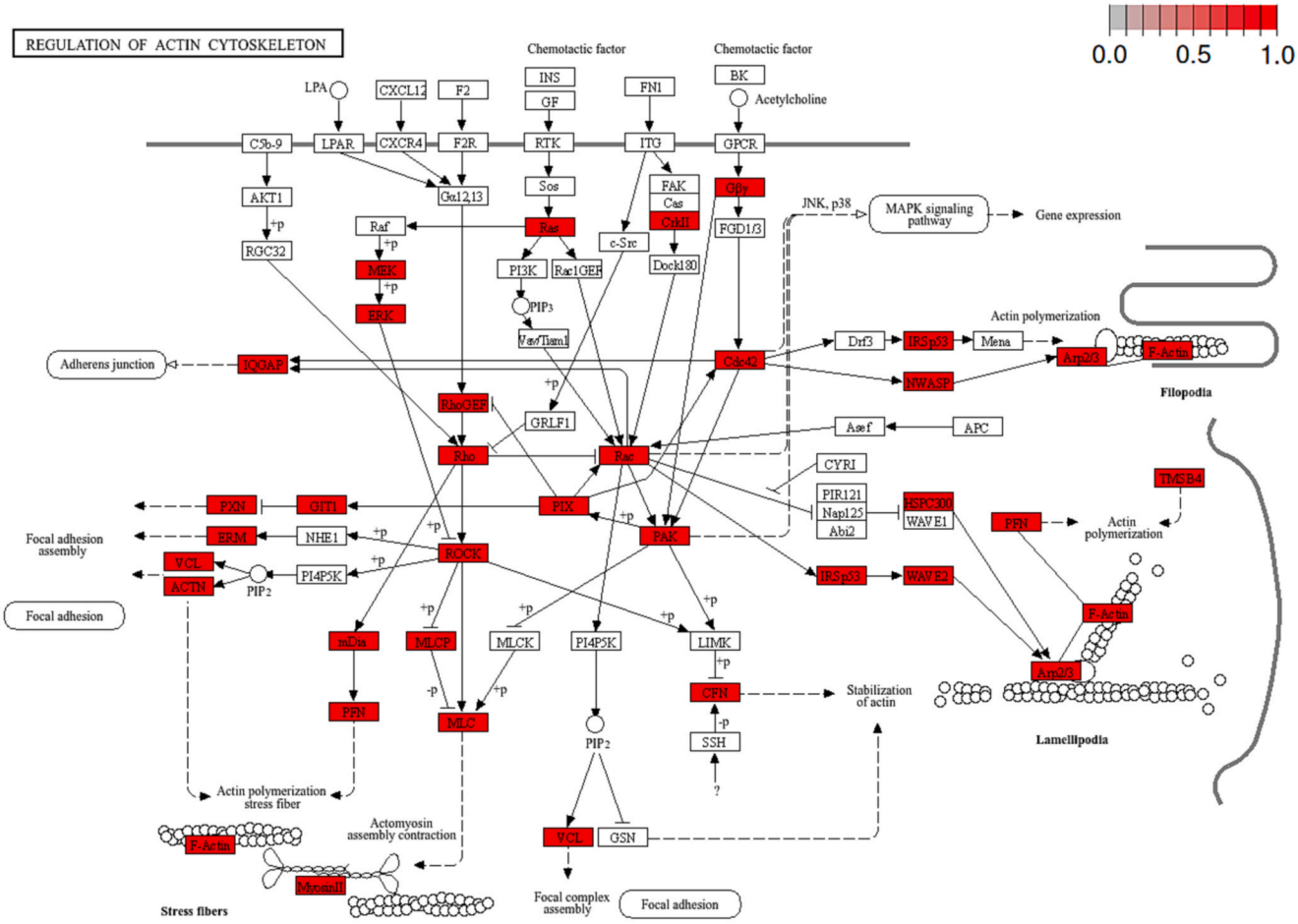

Fig. 12. Proteins captured by AA9p involved in the regulation of actin cytoskeleton pathway.

form of TG2 interacted more extensively with BID. Overall, the Z-scores were quite similar across the different simulations, suggesting that all docking configurations (for both BID and BAX) were relatively balanced in terms of quality, but the closed conformation of TG2 shows slightly more favourable scores for BID.

To confirm the interaction with these proteins, we carried out immunoprecipitation experiments. As shown in Figs. 16D and 15E, using anti-BID antibodies, we found not only BID itself but also TG2 in the immunoprecipitates. However, BID was not identified when the reaction was performed using anti-TG2 antibodies, in which case the presence of BAX was instead detectable. Notably, densitometric analysis (Fig. 16E) shows that the enrichment levels observed for the Ab-TG2/BAX and Ab-BID/TG2 conditions are overall comparable, further supporting that both interactions occur, albeit with different detectability depending on the immunoprecipitation conditions.

3.6. Based on the morphological changes, TEM provides evidence of ferroptosis induced by AA9

Aiming to analyze whether the effects of treatment of breast cancer cells with AA9 were consistent with ferroptosis or other forms of cell death using TEM, we analyzed the morphology of cells treated with the inhibitor alone or in combination with ferrostatin-1, a well-known inhibitor of ferroptosis [48]. The morphological changes are depicted in Fig. 17. Control cells showed mitochondria with preserved morphology, well-organized mitochondrial cristae, intact membranes, and no signs of cytoplasmic damage. In contrast, cells treated with AA9 exhibited ultrastructural alterations typical of ferroptosis, including reduced mitochondria, marked matrix thickening, cristae reduction/rarefaction, a more electron-dense mitochondrial appearance, and relative preservation of the nuclear membrane (absence of typical apoptosis). Nuclear condensation typical of apoptosis, formation of apoptotic bodies, or marked cytoplasmic vacuolization typical of necrosis were not observed. Therefore, the pattern induced by AA9 treatment is consistent with the ultrastructural phenotype described for ferroptosis. TEM analysis of cells treated with DMSO (the vehicle) shows that it does not induce detectable ultrastructural alterations in MDA-MB-436 cells, confirming that the phenotype observed after treatment with AA9 is not attributable to the solvent but to TG2 inhibition. In the combined treatment with 1 μM ferrostatin-1, mitochondrial alterations are attenuated, with mitochondria more similar to controls with less matrix thickening, revealing a clear morphological “rescue” effect.

In high-magnification images (penultimate row, 17,500x–28,000x), electron-dense granules consistent with intracellular iron deposits or ferruginous aggregates appear near the mitochondria. These granules appear consistent with iron/ferritin accumulations or iron-protein complexes, but are less frequent or less evident in samples treated with ferrostatin-1 and in control samples. Their presence in AA9 treatment suggests an alteration in iron homeostasis, perhaps an increase in the labile iron pool, which is, in any case, highly consistent with a ferroptotic phenotype.

Similar experiments carried out also in MDA-MB-231 cells clearly support ferrostatin-1-mediated morphological protection against AA9-induced damage.

These findings suggest that AA9-induced damage is ferroptosis-dependent, and ferrostatin-1 (lipid peroxidation inhibitor) prevents its

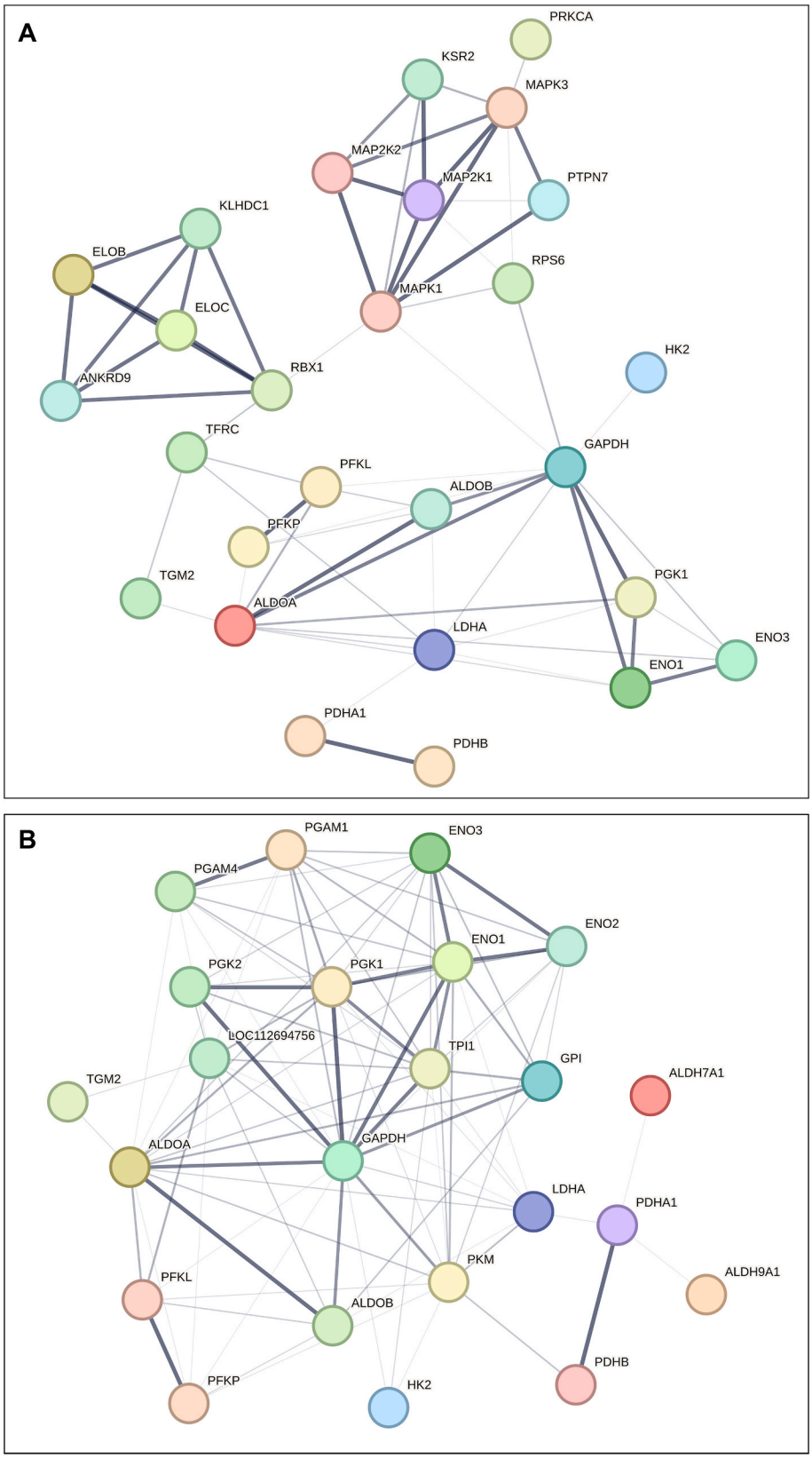

Fig. 13. Proteins target of AA9p interacting physically with TG2. In A, proteins included in hypoxia; in B, in glycolysis.

morphological phenotype.

4. Discussion

In this study, we provide evidence that the inhibition of TG2 by two structurally distinct irreversible inhibitors, Z-DON and AA9, consistently

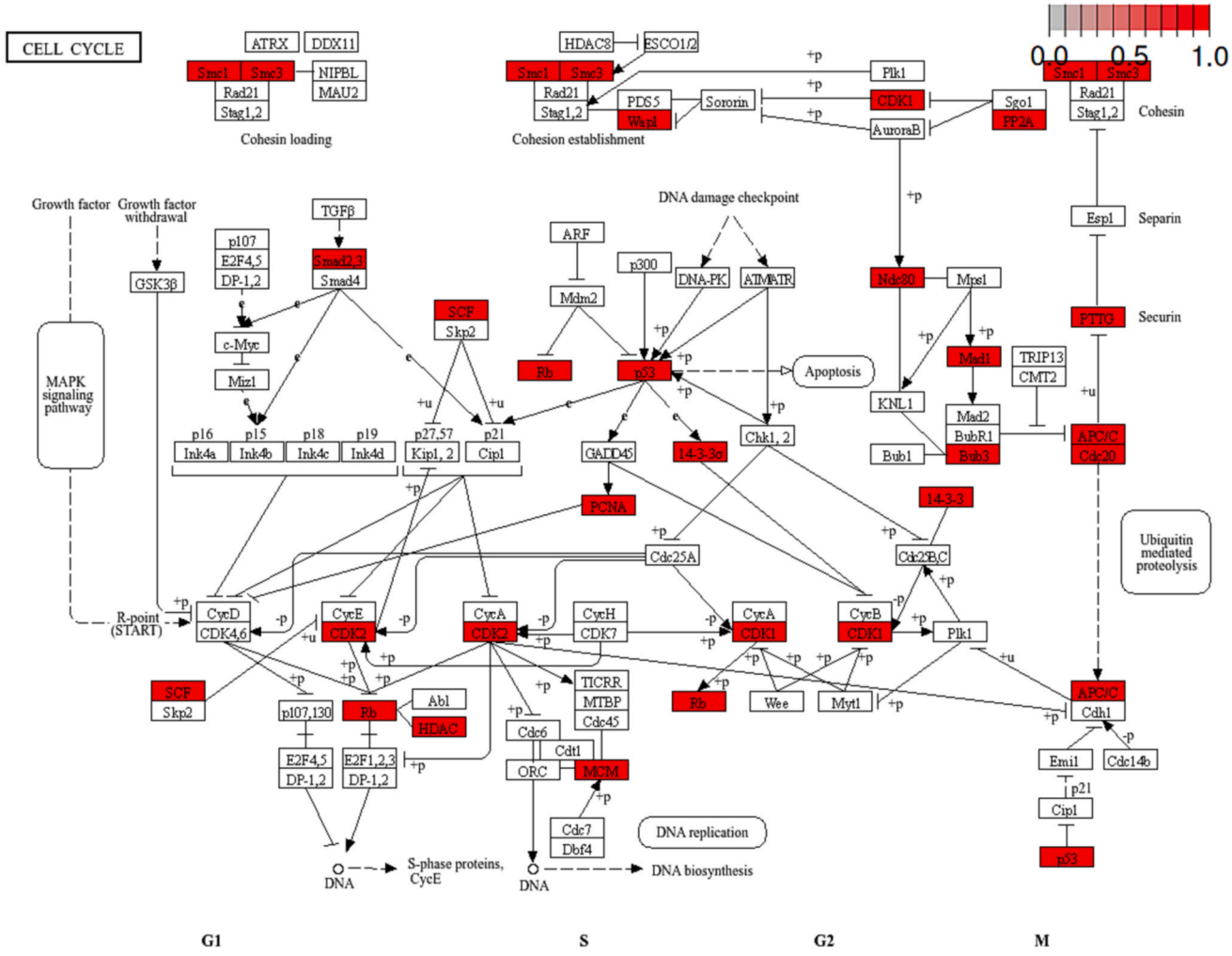

Fig. 14. Proteins captured by AA9p involved in the cell cycle.

drives transcriptional programs associated with ferroptosis across cell types of different origin. It should be noted that, in macrophage datasets, ferroptosis was inferred based on transcriptomic enrichment and was not directly validated at the functional level. By integrating RNA-sequencing datasets from macrophage populations [15] and breast cancer cells [11], we identified a conserved set of 137 deregulated genes following TG2 inhibition. Functional enrichment unequivocally pointed out ferroptosis as the only pathway significantly shared across all conditions and STRING network analysis revealed key ferroptosis-related genes (*HMOX1*, *FTL*, *SLC7A11*, *GCLM*, *MAP1LC3B*, and *TXNRD1*) as central nodes within the TG2-regulated network. Furthermore, the identification of *MAP1LC3B* and *HMOX1* as shared deregulated genes across independent TG2-targeting strategies and tumour types is consistent with the results of ORA performed on datasets from SW480 and HCT116 CRCs, in which TG2 knockdown was achieved using shRNAs and shRNA or CRISPR/Cas9 [31]. These genes converge on iron metabolism, GSH metabolism, and ROS detoxification, three crucial pillars that determine ferroptosis susceptibility [38,49].

In this context, it is important to consider that epithelial–mesenchymal transition (EMT), a key driver of tumour progression, invasiveness, and therapy resistance, is tightly linked to redox signalling pathways, particularly those mediated by hydrogen peroxide (H_2O_2). Beyond its role as a by-product of oxidative stress, H_2O_2 functions as a signalling molecule capable of inducing oxidative post-translational modifications, especially on cysteine residues, thereby modulating protein activity and intracellular signalling networks. During EMT, increased ROS and H_2O_2 levels promote metabolic rewiring and cellular plasticity, enabling tumour adaptation to hostile microenvironments [50]. Notably, TG2 itself is a redox-sensitive protein whose activity and conformational state are regulated by oxidative conditions, positioning it as a potential integrator of redox signalling and cellular stress responses. Importantly, the redox imbalance associated with EMT also creates a state of heightened vulnerability, as these cells become increasingly dependent on antioxidant systems such as GSH metabolism, thereby rendering them more susceptible to ferroptosis. In this framework, TG2 inhibition may exploit this redox liability, contributing to the ferroptotic phenotype observed in our experimental models, as a node linking EMT, ROS, and ferroptosis.

We focused on AA9 rather than Z-DON because of its predicted higher selectivity for TG2, which consistently emerged as the top-ranked target across three independent bioinformatic platforms. We therefore chose AA9, focusing on breast cancer cellular models, particularly those representatives of clinically aggressive subtypes characterized by a high likelihood of recurrence and a lack of effective targeted therapies [37]. Despite their distinct genetic backgrounds, both cell lines employed exhibited a coherent ferroptotic response to AA9, with upregulation of *HMOX1* [51], *FTH1* [52], and *CHAC1* [53], together with the down-regulation of *GPX4* and *GSS*, key components of the cellular anti-ferroptotic machinery [54]. These transcriptional changes were corroborated by protein-level validation of HMOX1 and FTH1, further

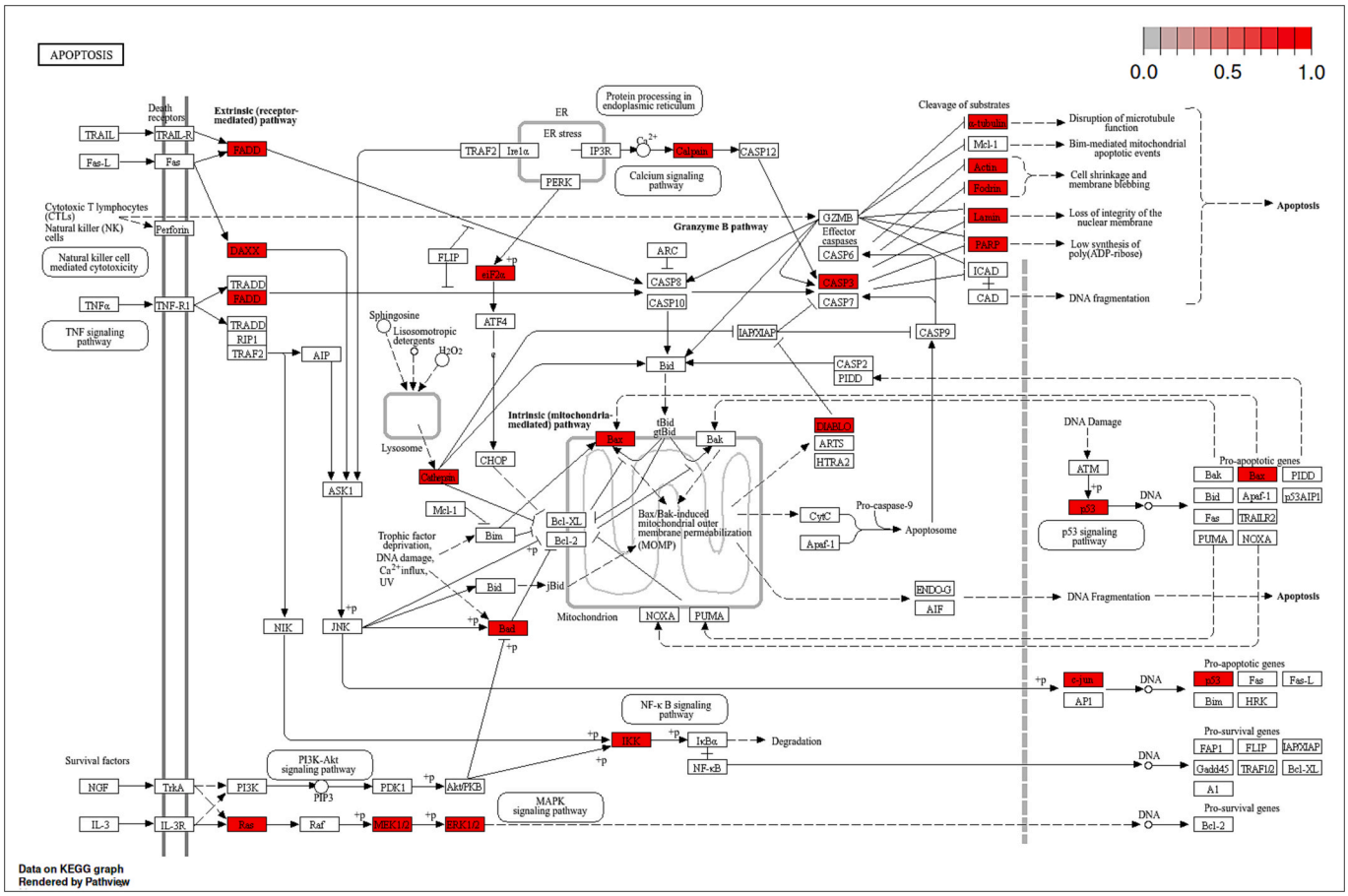

Fig. 15. Proteins captured by AA9p involved in the apoptosis.

reinforcing the link between TG2 inhibition and ferroptotic stress. However, AA9 treatment induced AKT2 phosphorylation at Ser474, indicative of mTORC2 activation [55], suggesting a compensatory attempt to preserve metabolic and redox homeostasis [56]. However, this adaptive response appears ineffective, as evidenced by the upregulation of CHAC1, a driver of GSH degradation and marker of redox buffering failure [57], indicating that cells ultimately fail to restore redox balance. Consistently, GPX4 depletion, recognized as a hallmark of ferroptotic collapse [48], further supports the establishment of an irreversible ferroptotic state. The mechanistic link between TG2 activity and the observed metabolic and ferroptotic alterations was confirmed by TG2 silencing experiments, which partially recapitulated the transcriptional effects induced by AA9. In particular, modulation of *ALDOA* and *GPX4* expression was observed following siRNA transfection, supporting a direct role of TG2 in regulating both metabolic reprogramming and redox homeostasis. Decreased levels of *GPX4* are consistent with a ferroptosis-permissive environment, likely driven by impaired GSH availability and increased oxidative stress, whereas the concomitant alteration of *ALDOA* suggests a broader impact on glycolytic flux and metabolic plasticity. Within this framework, TG2 may act as a critical integrative node linking redox–metabolic crosstalk.

This is consistent with an impaired cystine/glutamate exchange and decrease in GSH, as detected by Gallo *et al.* [12], who described GSH and cystathionine depletion with intracellular glutamate accumulation, representing a metabolic ferroptotic signature [58]. TG2 inhibition also induced metabolic rewiring [12], concomitant collapse of NAD^+ homeostasis, and impact on glycolysis, including lower lactate levels. In our experiments, the changes in gene expression of glycolytic enzymes (*ENO1* and *LDHA*) suggest a decrease in glycolytic flux, although the enhanced expression of *ALDOA* implies a corrective measure at metabolic reprogramming. Indeed, ALDOA has emerged with non-canonical roles in cancer biology [59], extending beyond glycolysis to include regulation of cytoskeletal dynamics and stress adaptation. In breast carcinoma, higher ALDOA levels have been linked to improved metastasis-free survival [60]. It could be an interesting player associated with TG2 in the HIF and glycolysis networks, as supported by our "fishing" experiments with AA9p.

The metabolic analyses revealed an early rise in intracellular ATP, followed by its decline and possibly concomitant release into the extracellular space. This biphasic ATP trend may reflect an initial compensatory phase preceding ferroptotic membrane damage and ATP release. Notably, the lack of metabolic alterations induced by the cell-impermeable inhibitor NCEG2 reinforces the hypothesis that intracellular TG2 activity is required to trigger these effects.

AA9 also affected cell cycle regulation in MDA-MB-231 cells, leading to a decrease in CCNB1, which prevents proper formation of the CCNB1/CDK1 complex, and to a marked delay in S-phase progression with an impaired S-to-G2 transition, resulting in S-phase accumulation. The concomitant decrease in CDKN1B may facilitate S-phase entry through enhanced CDK activity, thereby increasing the fraction of cells engaged in a replication program that cannot be completed. This cellular profile resembles that induced by agents causing replication stress or DNA damage, such as DNA polymerase or checkpoint kinase inhibitors. In MDA-MB-436 cells, we observed an increase in *CDKN1A*, consistent with G0/G1 accumulation, a response commonly associated with oxidative stress–induced growth arrest and apoptotic signalling [61]. These cell cycle perturbations are tightly linked to the redox imbalance and ferroptotic stress triggered by TG2 inhibition. ROS accumulation and GSH depletion are well known to interfere with DNA replication fidelity and checkpoint control, thereby coupling metabolic collapse to proliferative

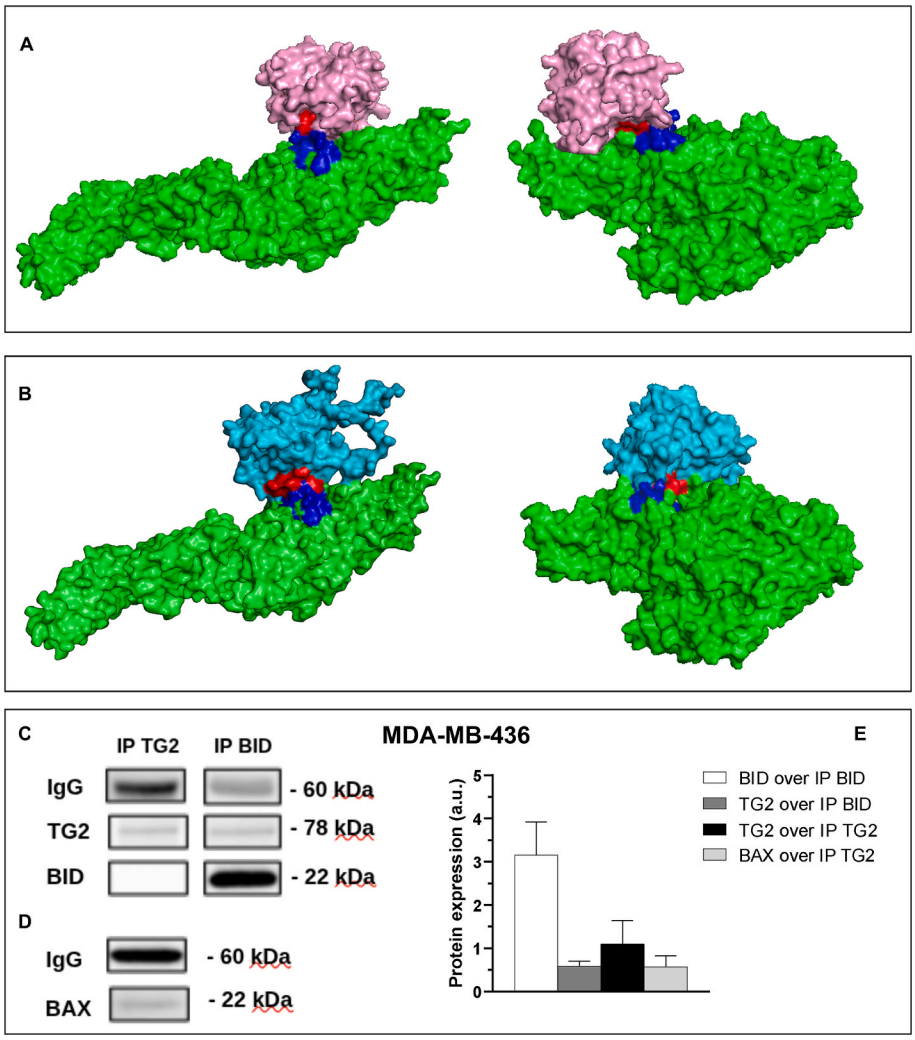

Fig. 16. BH3 domain of TG2 and interaction partners BID and BAX. In A and B, the molecular docking models showing the interaction of BID (Cyan) or BAX (Pink) with TG2 (Green), respectively. The BH3 domains of BID or BAX and TG2 are highlighted in Red and Blue respectively. In C and D, the coimmunoprecipitation of endogenous TG2, BID and BAX in MDA–MB–436 cells using antibodies against TG2 or BID (IP TG2, IP BID). IgG was blotted as a control for equal antibody addition to samples and molecular weights are indicated on the right side. In E, densitometric quantification of co–immunoprecipitated proteins from panel C and graphical normalization of TG2, BID and BAX, expressed as arbitrary units (a.u.). All the data are represented as mean of three independent experiments; bars represent mean ± SD.

arrest [62]. In this context, AKT2 phosphorylation does not reflect an effective pro-survival program but rather an abortive compensatory response that fails to counteract ferroptotic progression.

To identify the molecular targets of AA9, we developed an *in vitro* capture strategy based on a propargylated analogue (AA9p), which retained inhibitory activity toward TG2 while enabling bioorthogonal tagging and enrichment of interacting proteins. Such probe-based strategies fall within the broader framework of activity-based protein profiling, which enables functional interrogation of enzyme activity and target engagement in complex biological systems [44]. Proteomic profiling combined with ORA confirmed TG2 as the principal target and revealed enrichment of KEGG pathways related to chaperone systems, cytoskeletal dynamics, and cell cycle and apoptotic regulation (including BAX), outlining a coordinated stress-adaptation network destabilized by TG2 inhibition.

These findings also suggest that the characterized proteins may include not only TG2 interactors but also off-targets associated with AA9p, potentially contributing to the observed biological effects. Although Histone deacetylase 1 (HDAC1), included in the cell cycle pathway, emerged as a potential secondary target, its lower prediction scores and the observed transcriptional patterns argue against its dominant contribution (particularly the downregulation of *CDKN1B*, typically upregulated by HDAC1 inhibition [63,64]). Nevertheless, note that HDAC1 inhibitors generally induce the expression of pro-apoptotic genes [65], which in any case are consistent with the desired cytotoxic effects on tumour cells.

Finally, we explored the crosstalk between ferroptosis and apoptosis. BID acts mainly as an apoptotic initiator, whereas BAX, already reported to bind the BH3-like motif of TG2 [20], contributes to both pathways through mitochondrial membrane permeabilization, highlighting their role in cell death regulation [43,46]. Docking analysis revealed distinct interaction patterns between TG2 and the pro-apoptotic proteins BID and BAX depending on the conformational state of TG2. The closed conformation (cTG2) exhibited the most favourable interaction with BID, as indicated by the lowest HADDOCK score and the largest buried surface area, suggesting the formation of a stable and extensive interface. In contrast, BAX showed a preference for the open conformation of TG2 (oTG2), displaying a more favourable docking score compared to the closed state. Although electrostatic contributions were prominent in some complexes, the overall binding appeared to be driven by a balance of intermolecular interactions and interface complementarity. These findings indicate that TG2 may engage BID and BAX through

Table 3
Docking score obtained by HADDOCK v2.4 software. The top-ranking cluster for each complex in terms of HADDOCK score, cluster size, RMSD from the lowest energy structure, intermolecular van der Waals and electrostatic energies, desolvation and restraint violation energies, buried surface area, and Z-score as a measure of complex quality. The table compares the closed TG2 (cTG2)–BID, open TG2 (oTG2)–BID, cTG2–BAX, and oTG2–BAX complexes, with more negative HADDOCK scores and larger buried surface areas indicating more favourable and extensive protein–protein inferred interfaces.

Docking scores	*cTG2-BID	*oTG2-BID	*cTG2-BAX	*oTG2-BAX
HADDOCK score	−77.7 ± 2.8	−68.4 ± 5.4	−66.7 ± 2.1	−75.1 ± 5.2
Cluster size	8	23	74	42
RMSD from the overall lowest energy structure	9.3 ± 0.7	15.6 ± 0.4	11.7 ± 0.1	2.4 ± 2
Van der Waals energy	−44.2 ± 4.2	−17.6 ± 8.6	−28.1 ± 3.8	−38.8 ± 6
Electrostatic energy	−262.7 ± 37.8	−337.5 ± 28.7	−274.4 ± 33	−221.6 ± 29.3
Desolvation energy	13.5 ± 4.5	9.8 ± 2.3	9.6 ± 3.6	3.4 ± 2.6
Restraints violation energy	54.5 ± 27.4	68.5 ± 39.9	66.7 ± 17.2	46.9 ± 26.1
Buried surface area	1993.3 ± 56.5	932.7 ± 38.3	1129.9 ± 42.5	1179.0 ± 161
Z-score	−1.5	−1.9	−1.5	−1.6

*cTG2 (closed structure TG2); oTG2 (open structure TG2).

conformation-dependent mechanisms, potentially reflecting distinct roles in apoptotic signalling pathways. However, these results are based on computational predictions and require further experimental validation.

Co-immunoprecipitation experiments revealed an asymmetric detection of the TG2–BID interaction, as TG2 was efficiently recovered following immunoprecipitation with anti-BID antibody, whereas BID was not readily detected in anti-TG2 precipitates. This discrepancy does not necessarily exclude an interaction, but may reflect the multifunctional nature of TG2, which engages in multiple protein complexes, such that only a limited fraction of total TG2 is associated with BID under these experimental conditions. In contrast, the TG2–BAX interaction appeared more readily detectable, suggesting a more stable association or a larger fraction of TG2 involved in complexes containing BAX.

We hypothesize that the open TG2 conformation may be more directly involved in apoptosis, potentially modulating cytochrome *c* release, whereas the closed form may exert a protective, regulatory role. By acting as a linker between ferroptosis and apoptosis, BID could help explain how this inhibitor impacts both processes.

In this context, we underline that AA9 can react with conformationally dynamic TG2, locking it in its open conformation [66]. Recent evidence indicates that irreversible inhibitors targeting TG2 have been shown not only to block its enzymatic function, but also to induce a shift in its conformational equilibrium. Nε-acryloyllysine piperazides, for instance, promote a persistent conformational remodelling of TG2, effectively altering its structural dynamics and potentially its interaction profile [67]. Hence, TG2 inhibition should be viewed not only as enzymatic inactivation, but also as a mechanism capable of reshaping TG2-dependent signalling networks.

Additional studies are needed to determine whether the combined use with ferroptosis inhibitors [68] may counteract the effects of AA9. The protective effect of ferrostatin-1 when administered in co-treatment with AA9, as demonstrated by TEM analysis in MDA-MB-436 cells, reveals an intriguing aspect which may guide future treatment options to be further explored.

Our data support the view that ferroptosis represents the primary and initiating mechanism triggered by TG2 inhibition. The profound disruption of GSH metabolism and iron homeostasis establishes a ferroptotic collapse that precedes and likely drives a secondary drift toward apoptotic signalling, culminating in terminal cell death. In this framework, apoptosis and cell cycle arrest appear not as the dominant initiating pathways, but as a downstream consequence of ferroptotic stress and mitochondrial dysfunction.

The use of a cell-permeable, irreversible TG2 inhibitor, AA9, demonstrates that intracellular TG2 plays a central role in maintaining redox balance, metabolic adaptability, and resistance to ferroptotic stress in aggressive breast cancer cells. Consistent with these observations, TG2 has been widely implicated in breast cancer progression, where it promotes EMT, metastatic dissemination, and resistance to therapy through the regulation of redox homeostasis and stress adaptation pathways, further supporting its role as a key determinant of tumour cell survival under conditions that overlap with ferroptosis-related vulnerability [69]. Interestingly, CTCs, especially the epiB and mesenchymal subgroups, were positioned close to trophectoderm-like and metastatic transcriptional states, supporting the idea that these populations may represent highly plastic and metastasis-competent intermediates [9]. Although TG2 was not a central mechanistic focus of the study, the predominance of breast cancer-derived CTCs in the dataset and the known association of TG2 with epithelial-mesenchymal plasticity, metastasis, and drug resistance make TG2 an attractive candidate for further investigation in CTC biology. Also, it will be of considerable interest to determine whether TG2 inhibitors can impair these features in aggressive CTC subsets.

Emerging evidence supports a functional interplay between TG2 and ferroptosis-related pathways in other tumour contexts. In glioma cells, the ferroptosis inducer RSL3 has been shown to enhance radiosensitivity while concurrently downregulating TG2, identifying this enzyme as a determinant of therapy resistance [70]. Mechanistically, RSL3 promotes oxidative stress that triggers glutathione *S*-transferase P1-dependent *S*-glutathionylation of TG2, leading to its proteasomal degradation. This results in impaired nuclear accumulation of TG2 following ionizing radiation and disruption of its interaction with topoisomerase IIα, compromising DNA damage repair. In addition, suppression of *TGM2* gene attenuates EMT, further contributing to reduced tumour cell adaptability and survival. Notably, genetic modulation of TG2 recapitulates these effects, as its knockdown sensitizes glioma cells to radiation, whereas its overexpression mitigates the impact of RSL3. While ferroptosis inhibition only partially rescues cell viability in this setting, these findings indicate that TG2 operates at the intersection of oxidative stress responses, ferroptosis-associated signalling, and resistance mechanisms. In line with our model, these observations further support the notion that disruption of TG2 function may compromise redox homeostasis and stress adaptation, thereby lowering the threshold for ferroptotic susceptibility and simultaneously impairing pro-survival pathways such as DNA repair and EMT, common processes that underlie therapy resistance across different cancer types.

By inducing a coordinated ferroptotic transcriptional, metabolic, and ultrastructural phenotype, AA9 provides proof-of-concept that TG2 represents a druggable node linking hypoxia signalling, GSH metabolism, iron handling, mitochondrial integrity, and cell cycle control. Given the emerging role of ferroptosis in cancer therapy resistance, these findings position TG2 as a pharmacologically actionable modulator of ferroptosis susceptibility, providing a rationale for the development of TG2-targeting strategies, either through optimized inhibitors or in combination with ferroptosis-inducing agents, as a potential approach to overcome metabolic plasticity and drug tolerance in TNBC.

CRediT authorship contribution statement

Pietro Ancona: Writing – review & editing, Writing – original draft, Software, Investigation, Formal analysis, Conceptualization. **Silvia Grassilli:** Visualization, Validation, Methodology, Investigation. **Cristina Zuccato:** Validation, Methodology, Investigation. **Cinzia Brenna:** Validation, Methodology. **Davide Barboni:** Software, Methodology. **Alberto Cavazzini:** Resources, Project administration. **Martina Catani:**

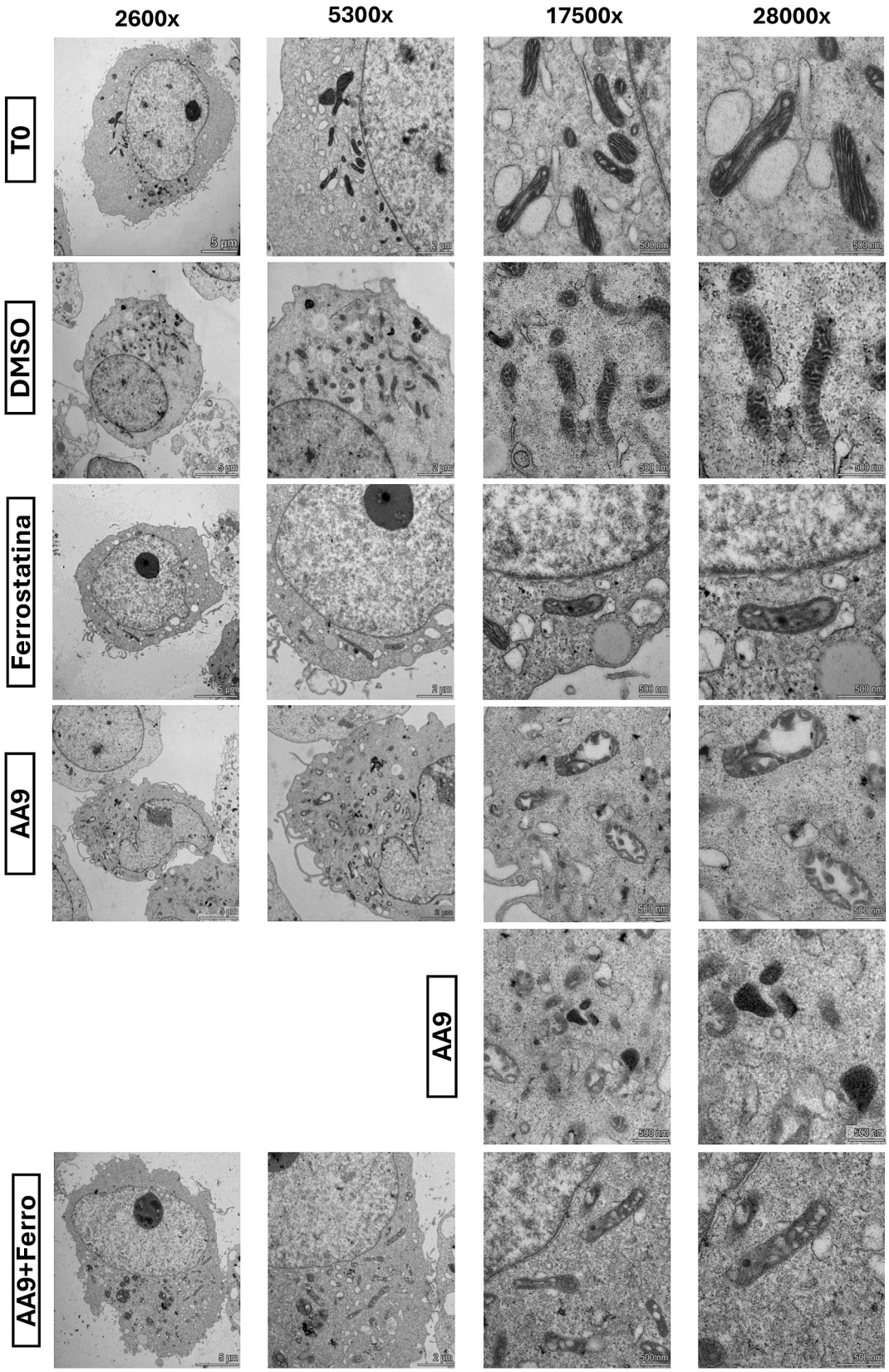

Fig. 17. TEM analysis of morphological changes induced by AA9 in MDA-MB-436 cells. Cells were cultured in a T75 flask. Ferrostatin-1 treatment was performed at 1 μM for 2 h before the addition of 50 μM AA9, then maintained for the subsequent 48 h. The vehicle, DMSO, was used at 0.2%. TEM images acquired at different magnifications (2,600×, 5,300×, 17,500×, and 28,000 ×) showing the ultrastructural features of T0 control cells and cells treated with DMSO, ferrostatin-1, AA9, and combined treatment with ferrostatin-1 + AA9.

Visualization, Supervision. **Valeria Bertagnolo:** Visualization, Data curation. **Pauline Navals:** Writing – review & editing, Methodology, Investigation. **Jocelyn A. Menard:** Writing – review & editing, Methodology, Investigation, Formal analysis. **Jeffrey C. Smith:** Writing – review & editing, Supervision. **Carlo M. Bergamini:** Writing – review & editing, Writing – original draft, Validation, Supervision. **Nicoletta Bianchi:** Writing – review & editing, Writing – original draft, Supervision, Formal analysis, Data curation, Conceptualization. **Jeffrey W. Keillor:** Writing – review & editing, Writing – original draft, Visualization, Methodology. **Luca M. Neri:** Writing – review & editing, Data curation, Conceptualization.

Ethics approval

Not applicable.

Funding

This research was funded by Fondo Interdisciplinare per la Ricerca Dipartimentale (FIRD) 2025 (N.B.); Fondo di Ateneo per la Ricerca Scientifica (FAR) 2025 application ID 210043 (N.B.); the National Recovery and Resilience Plan (NRRP), Mission 04 Component 2 Investment 1.5 - NextGenerationEU, Call for tender n. 3277 dated December 30, 2021, Award Number: 0001052 dated June 23, 2022 (assigned to A.C.); D. Barboni benefits from a PhD scholarship financed by the Ministerial Decree no. 118 of 2nd March 2023, based on the NRRP - funded by the European Union - NextGenerationEU - Mission 4 “Education and Research”, Component 1 “Enhancement of the offer of educational services: from nurseries to universities” - Investment 4.1 “Extension of the number of research doctorates and innovative doctorates for public administration and cultural heritage” (assigned to M.C.); Italian MUR PNRR National Center for HPC, big data and quantum computing, M4C2, CUP: F77G22000120006 (P.A.).

Declaration of competing interest

The authors declare that they have no known competing financial interests or personal relationships that could have appeared to influence the work reported in this paper.

Acknowledgments

The authors acknowledge the use of the instruments at the Electron Microscopy Center of the University of Ferrara and the scientific and technical assistance of Dr. Paola Boldrini.

We gratefully thank Prof. Peggy Marconi and Dott. Mattia Buratto for their contributions to this project and for granting us access to the GloMax® Discover instrument.

Data availability

Proteomics data are accessible at: https://docs.google.com/spreadsheets/d/1C6xzq3q8WHAeUmNx6hG5sUyPTFQKFOyt/edit?usp=-drive_link&ouid=112878060347254043013&rtpof=true&sd=true

References

[1] G. Huang, Y. Cai, M. Ren, X. Zhang, Y. Fu, R. Cheng, et al., Salidroside sensitizes triple-negative breast cancer to ferroptosis by SCD1-mediated lipogenesis and NCOA4-mediated ferritinophagy, J. Adv. Res. 74 (2025) 589–607.
[2] F. Yang, Y. Xiao, J.H. Ding, X. Jin, D. Ma, D.Q. Li, et al., Ferroptosis heterogeneity in triple-negative breast cancer reveals an innovative immunotherapy combination strategy, Cell Metab. 35 (1) (2023) 84–100.e8.
[3] X. Yao, R. Xie, Y. Cao, J. Tang, Y. Men, H. Peng, et al., Simvastatin induced ferroptosis for triple-negative breast cancer therapy, J. Nanobiotechnology 19 (1) (2021) 311.
[4] M. Gagliardi, V. Saverio, F. Rossin, M. D'Eletto, M. Corazzari, Transglutaminase 2 and ferroptosis: a new liaison? Cell Death Discov. 9 (1) (2023) 88.
[5] E. Zaltron, F. Vianello, A. Ruzza, A. Palazzo, V. Brillo, I. Celotti, et al., The role of transglutaminase 2 in cancer: an update, Int. J. Mol. Sci. 25 (5) (2024) 2797.
[6] F. Rossin, M. D'Eletto, D. Macdonald, M.G. Farrace, M. Piacentini, TG2 transamidating activity acts as a reostat controlling the interplay between apoptosis and autophagy, Amino Acids 42 (2012) 1793–1802.
[7] L.A. Farrelly, R.E. Thompson, S. Zhao, A.E. Lepack, Y. Lyu, N.V. Bhanu, et al., Histone serotonylation is a permissive modification that enhances TFIID binding to H3K4me3, Nature 567 (7749) (2019) 535–539.
[8] N. Bianchi, F. Brugnoli, S. Grassilli, K. Bourgeois, J.W. Keillor, C.M. Bergamini, et al., The motility and mesenchymal features of breast cancer cells correlate with the levels and intracellular localization of transglutaminase type 2, Cells 10 (11) (2021) 3059.
[9] S. Volinia, A. Terrazzan, T.S. Kaminski, K. Jadzewski, E. Reali, N. Bianchi, et al., Circulating tumour cells share RNA modules with early embryo trophectoderm and with metastatic cancer, Cancer Commun. (Lond) 45 (5) (2025) 500–504.
[10] E.W.J. Gates, N.D. Calvert, N.J. Cundy, F. Brugnoli, P. Navals, A. Kirby, et al., Cell-impermeable inhibitors confirm that intracellular human transglutaminase 2 is responsible for the transglutaminase-associated cancer phenotype, Int. J. Mol. Sci. 24 (16) (2023) 12546.
[11] P. Ancona, A. Trentini, A. Terrazzan, S. Grassilli, P. Navals, E.W.J. Gates, et al., Transcriptomics studies reveal functions of transglutaminase 2 in breast cancer cells using membrane permeable and impermeable inhibitors, J. Mol. Biol. 436 (10) (2024) 168569.
[12] M. Gallo, E. Ferrari, A. Terrazzan, F. Brugnoli, A. Spisni, C. Taccioli, et al., Metabolic characterisation of transglutaminase 2 inhibitor effects in breast cancer cell lines, FEBS J. 290 (22) (2023) 5411–5433.
[13] Z. Yang, W. Su, X. Wei, S. Qu, D. Zhao, J. Zhou, et al., HIF-1α drives resistance to ferroptosis in solid tumours by promoting lactate production and activating SLC1A1, Cell Rep. 42 (8) (2023) 112945.
[14] X. Gao, W. Hu, D. Qian, X. Bai, H. He, L. Li, S. Sun, The Mechanisms of ferroptosis under hypoxia, Cell Mol. Neurobiol. 43 (7) (2023) 3329–3341.
[15] Y. Shinoda, H. Tatsukawa, A. Yonaga, R. Wakita, T. Takeuchi, T. Tsuji, et al., Tissue transglutaminase exacerbates renal fibrosis via alternative activation of monocyte-derived macrophages, Cell Death Dis. 14 (2) (2023) 136.
[16] A. Dobin, C.A. Davis, F. Schlesinger, J. Drenkow, C. Zaleski, S. Jha, et al., STAR: ultrafast universal RNA-seq aligner, Bioinformatics 29 (1) (2013) 15–21.
[17] M.I. Love, W. Huber, S. Anders, Moderated estimation of fold change and dispersion for RNA-seq data with DESeq2, Genome Biol. 15 (12) (2014) 550.
[18] J.M. Elizarraras, Y. Liao, Z. Shi, Q. Zhu, A.R. Pico, B. Zhang, WebGestalt 2024: faster gene set analysis and new support for metabolomics and multi-omics, Nucleic Acids Res. 52 (W1) (2024) W415–W421.
[19] D. Szklarczyk, R. Kirsch, M. Koutrouli, K. Nastou, F. Mehryary, R. Hachilif, et al., The STRING database in 2023: protein-protein association networks and functional enrichment analyses for any sequenced genome of interest, Nucleic Acids Res. 51 (D1) (2023) D638–D646.
[20] C. Rodolfo, E. Mormone, P. Matarrese, F. Ciccosanti, M.G. Farrace, E. Garofano, et al., Tissue transglutaminase is a multifunctional BH3-only protein, J. Biol. Chem. 279 (52) (2004) 54783–54792.
[21] P. Tedeschi, F. Brugnoli, S. Merighi, S. Grassilli, M. Nigro, M. Catani, et al., The effect of different storage conditions on phytochemical composition, shelf-life, and bioactive compounds of Voghiera Garlic PDO, Antioxidants (Basel) 12 (2) (2023) 499.
[22] C. Mamat, M. Pretze, M. Gott, M. Köckerling, Synthesis, dynamic NMR characterization and XRD studies of novel *N,N'*-substituted piperazines for bioorthogonal labelling, Beilstein J. Org. Chem. 12 (2016) 2478–2489.
[23] R. Wodtke, J. Steinberg, M. Köckerling, R. Löser, C. Mamat, NMR-based investigations of acyl-functionalized piperazines concerning their conformational behavior in solution, RSC Advances 8 (71) (2018) 40921–40933.
[24] C. Koenig, A. Martinez-Val, P. Naicker, S. Stoychev, J. Jordaan, J.V. Olsen, Protocol for high-throughput semi-automated label-free- or TMT-based phosphoproteome profiling, STAR Protoc. 4 (2023) 102536.
[25] D.A. Wallace, S. Tribe, P. Navals, C. Bi, T. Sharma, J.W. Keillor, Structure–activity relationships of hydrophobic small molecule irreversible inhibitors of tissue transglutaminase, RSC Med. Chem. 17 (1) (2025) 422–451.
[26] A. Leblanc, C. Gravel, J. Labelle, J.W. Keillor, Kinetic studies of guinea pig liver transglutaminase reveal a general-base-catalyzed deacylation mechanism, Biochemistry 40 (28) (2001) 8335–8342.
[27] L.K. Pino, B.C. Searle, J.G. Bollinger, B. Nunn, B. MacLean, M.J. MacCoss, The Skyline ecosystem: Informatics for quantitative mass spectrometry proteomics, Mass Spectrom. Rev. 39 (3) (2020) 229–244.
[28] A.T. Kong, F.V. Leprevost, D.M. Avtonomov, D. Mellacheruvu, A.I. Nesvizhskii, MSFragger: ultrafast and comprehensive peptide identification in mass spectrometry-based proteomics, Nat. Methods. 14 (5) (2017) 513–520.
[29] S. Tyanova, J. Cox, Perseus: a bioinformatics platform for integrative analysis of proteomics data in cancer research, Methods Mol. Biol. 1711 (2018) 133–148.
[30] I. Reinisch, H. Michenthaler, A. Sulaj, E. Moyschewitz, J. Krstic, M. Galhuber, et al., Adipocyte p53 coordinates the response to intermittent fasting by regulating adipose tissue immune cell landscape, Nat. Commun. 15 (2024) 1391.
[31] P. Malkomes, I. Lunger, E. Oppermann, K. Abou-El-Ardat, T. Oellerich, S. Günther, et al., Transglutaminase 2 promotes tumorigenicity of colon cancer cells by inactivation of the tumor suppressor p53, Oncogene 40 (25) (2021) 4352–4367.
[32] N.P.K. Mahayana, N.B.A.S.N.J.D. Sutanegara, M.D.P. Mahardana, D.M. Wihandani, In-silico study of rosmarinic acid rRoles in inhibiting breast cancer progression, BioMedicine 15 (1) (2025) 23–30.

[33] A. Daina, O. Michielin, V. Zoete, SwissTargetPrediction: updated data and new features for efficient prediction of protein targets of small molecules, Nucleic Acids Res. 47 (W1) (2019) W357–W364.
[34] M.J. Keiser, B.L. Roth, B.N. Armbruster, P. Ernsberger, J.J. Irwin, B.K. Shoichet, Relating protein pharmacology by ligand chemistry, Nat. Biotechnol. 25 (2) (2007) 197–206.
[35] Z.J. Yao, J. Dong, Y.J. Che, M.F. Zhu, M. Wen, N.N. Wang, et al., TargetNet: a web service for predicting potential drug–target interaction profiling via multi-target SAR models, J. Comput. Aided Mol. Des. 30 (5) (2016) 413–424.
[36] H. Heberle, G.V. Meirelles, F.R. da Silva, G.P. Telles, R. Minghim, InteractiVenn: a web-based tool for the analysis of sets through Venn diagrams, BMC Bioinform. 16 (1) (2015) 169.
[37] V.B. Varzaru, T. Vlad, R. Popescu, C.S. Vlad, A.E. Moatar, I.M. Cobec, Triple-negative breast cancer: molecular particularities still a challenge, Diagnostics (Basel) 14 (17) (2024) 1875.
[38] X. Chen, P.B. Comish, D. Tang, R. Kang, Characteristics and biomarkers of ferroptosis, Front. Cell Dev. Biol. 9 (2021) 637162.
[39] N. Bao, Z. Chen, B. Li, H. Yang, X. Li, Z. Zhang, Study on the mechanism of formononetin against hepatocellular carcinoma: regulating metabolic pathways of ferroptosis and cell cycle, Int. J. Mol. Sci. 26 (6) (2025) 2578.
[40] E.W.J. Gates, A. Prince-Hallée, Y. Heidari, A. Sedighi, J.W. Keillor, High-affinity fluorogenic substrate for tissue transglutaminase reveals enzymatic hysteresis, Biochemistry 62 (21) (2023) 3085–3095.
[41] J. Stamnaes, D.M. Pinkas, B. Fleckenstein, C. Khosla, L.M. Sollid, Redox regulation of transglutaminase 2 activity, J. Biol. Chem. 285 (33) (2010) 25402–25409.
[42] H.P. Lesch, M.U. Kaikkonen, J.T. Pikkarainen, S. Ylä-Herttuala, Avidin-biotin technology in targeted therapy, Expert Opin. Drug. Deliv. 7 (5) (2010) 551–564.
[43] S. Hauser, P. Sommerfeld, J. Wodtke, C. Hauser, P. Schlitterlau, J. Pietzsch, et al., Application of a fluorescence anisotropy-based assay to quantify transglutaminase 2 activity in cell lysates, Int. J. Mol. Sci. 23 (9) (2022) 4475.
[44] E.O.J. Porta, P.G. Steel, Activity-based protein profiling: A graphical review, Curr. Res. Pharmacol. Drug Discov. 5 (2023) 100164.
[45] S. Neitemeier, A. Jelinek, V. Laino, L. Hoffmann, I. Eisenbach, R. Eying, et al., BID links ferroptosis to mitochondrial cell death pathways, Redox Biol. 12 (2017) 558–570.
[46] Q. Tang, H. Chen, Z. Mai, H. Sun, L. Xu, G. Wu, Chen, et al., Bim- and Bax-mediated mitochondrial pathway dominates abivertinib-induced apoptosis and ferroptosis, Free Radic. Biol. Med. 180 (2022) 198–209.
[47] R. Canella, F. Brugnoli, M. Gallo, J.W. Keillor, A. Terrazzan, E. Ferrari, et al., A multidisciplinary approach establishes a link between transglutaminase 2 and the Kv10.1 voltage-dependent K^+ channel in breast bancer, Cancers (Basel) 15 (1) (2022) 178.
[48] C. Scarpellini, G. Klejborowska, C. Lanthier, B. Hassannia, T. Vanden Berghe, K. Augustyns, Beyond ferrostatin-1: a comprehensive review of ferroptosis inhibitors, Trends Pharmacol. Sci. 44 (12) (2023) 902–916.
[49] L. Galluzzi, I. Vitale, S.A. Aaronson, J.M. Abrams, D. Adam, P. Agostinis, et al., Molecular mechanisms of cell death: recommendations of the nomenclature committee on cell death 2018, Cell Death Differ. 25 (3) (2018) 486–541.
[50] A.V. Milton, D.B. Konrad, Epithelial-mesenchymal transition and H_2O_2 signaling - a driver of disease progression and a vulnerability in cancers, Biol. Chem. 403 (4) (2022) 377–390.
[51] S.K. Chiang, S.E. Chen, L.C. Chang, A dual role of Heme Oxygenase-1 in cancer cells, Int. J. Mol. Sci. 20 (1) (2018) 39.
[52] D. Tang, X. Chen, R. Kang, G. Kroemer, Ferroptosis: molecular mechanisms and health implications, Cell Res. 31 (2) (2021) 107–125.
[53] J. Sun, H. Ren, J. Wang, X. Xiao, L. Zhu, Y. Wang, et al., CHAC1: a master regulator of oxidative stress and ferroptosis in human diseases and cancers, Front. Cell Dev. Biol. 12 (2024) 1458716.
[54] R. Brigelius-Flohé, M. Maiorino, Glutathione peroxidases, Biochim. Biophys. Acta 1830 (5) (2013) 3289–3303.
[55] A.L. Kearney, K.C. Cooke, D.M. Norris, A. Zadoorian, J.R. Krycer, D.J. Fazakerley, et al., Serine 474 phosphorylation is essential for maximal Akt2 kinase activity in adipocytes, J. Biol. Chem. 294 (45) (2019) 16729–16739.
[56] A. Szwed, E. Kim, E. Jacinto, Regulation and metabolic functions of mTORC1 and mTORC2, Physiol. Rev. 101 (3) (2021) 1371–1426.
[57] R.R. Crawford, E.T. Prescott, C.F. Sylvester, A.N. Higdon, J. Shan, M.S. Kilberg, et al., Human CHAC1 protein degrades glutathione, and mRNA induction is regulated by the transcription factors ATF4 and ATF3 and a bipartite ATF/CRE regulatory element, J. Biol. Chem. 290 (25) (2015) 15878–15891.
[58] J. Li, F. Cao, H. L. Yin, Z. J. Huang, Z. T. Lin, N. Mao, et al., Ferroptosis: past, present and future, Cell Death Dis. 11 (2020) (2) 88.
[59] S. Yu, Y. Xue, Y. Chen, Y. Cao, Y. Yang, X. Ge, et al., The multifaceted roles of aldolase A in cancer: glycolysis, cytoskeleton, translation and beyond, Hum. Cell 38 (2) (2025) 45.
[60] Y. Dai, Y. Yang, X. Li, G. Shi, T. Ni, Q. Zhu, et al., The expression and clinical significance of ALDOA in breast cancer Onco Targets Ther. 18 (2025) 845–862.
[61] K. Utama, N. Khamto, P. Meepowpan, P. Aobchey, J. Kantapan, J. Meerak, et al., 2',4'-Dihydroxy-6'–methoxy-3',5'-dimethylchalcone and its amino acid-conjugated derivatives induce G0/G1 cell cycle arrest and apoptosis via BAX/BCL2 ratio upregulation and in silico insight in SiHa cell lines, Eur. J. Pharm. Sci. 184 (2023) 106390.
[62] V. Mackova, M. Raudenska, H.H. Polanska, M. Jakubek, M. Masarik, Navigating the redox landscape: reactive oxygen species in regulation of cell cycle, Redox Rep. 29 (1) (2024) 2371173.
[63] S. Gu, Y. Tian, A. Chlenski, H.R. Salwen, Z. Lu, J.U. Raj, et al., Valproic acid shows a potent antitumour effect with alteration of DNA methylation in neuroblastoma, Anticancer Drugs 23 (10) (2012) 1054–1066.
[64] C. Draney, M.C. Austin, A.H. Leifer, C.J. Smith, K.B. Kener, T.J. Aitken, et al., HDAC1 overexpression enhances β-cell proliferation by down-regulating Cdkn1b/p27, Biochem. J. 475 (24) (2018) 3997–4010.
[65] R. Parveen, D. Harihar, B.P. Chatterji, Recent histone deacetylase inhibitors in cancer therapy, Cancer 129 (21) (2023) 3372–3380.
[66] A. Akbar, N.M.R. McNeil, M.R. Albert, V. Ta, G. Adhikary, K. Bourgeois, et al., Structure-activity relationships of potent, targeted covalent inhibitors that abolish both the transamidation and GTP binding activities of human tissue transglutaminase, J. Med. Chem. 60 (18) (2017) 7910–7927.
[67] A. Heerwig, A. Kick, P. Sommerfeld, S. Eimermacher, F. Hartung, M. Laube, et al., The impact of Nε-Acryloyllysine piperazides on the conformational dynamics of transglutaminase 2, Int. J. Mol. Sci. 24 (2) (2023) 1650.
[68] A.M. Battaglia, R. Chirillo, I. Aversa, A. Sacco, F. Costanzo, F. Biamonte, Ferroptosis and cancer: mitochondria meet the "Iron Maiden" cell death, Cells 9 (6) (2020) 1505.
[69] M. Li, X. Wang, J. Hong, J. Mao, J. Chen, X. Chen, et al., Transglutaminase 2 in breast cancer metastasis and drug resistance, Front. Cell. Dev. Biol. 12 (2024) 1485258.
[70] X. Wang, W. Shi, M. Li, Y. Xin, X. Jiang, RSL3 sensitizes glioma cells to ionizing radiation by suppressing TGM2-dependent DNA damage repair and epithelial-mesenchymal transition, Redox Biol. 78 (2024) 103438.